

# **Process-Induced Thermal and Viscoelastic Behavior of Extrusion Blow Molded Parts**

Esther Ramakers-van Dorp, Ph.D.

Doctoral Thesis Summary



**Tomas Bata University in Zlín**  
**Faculty of Technology**

*Doctoral Thesis Summary*

## **Process-Induced Thermal and Viscoelastic Behavior of Extrusion Blow Molded Parts**

**Procesem indukované tepelné a viskoelastické vlastnosti dílů  
vyrobených vytlačovacím vyfukováním**

Author:	<b>Esther Ramakers-van Dorp, Ph.D.</b>
Degree program:	P 3909 Process Engineering
Degree Course:	3909V013 Tools and Processes
Supervisor:	Prof. Ing. Berenika Hausnerová, Ph.D.
External examiners:	Prof. Giuseppe Titomanlio Doc. Petr Filip, CSc. Assoc. Prof. Vladimír Pavlínek, Ph.D.

Zlín, December 2019

© Esther Ramakers-van Dorp

Published by **Tomas Bata University in Zlín** in the Edition **Doctoral Thesis Summary**.

The publication was issued in the year 2019

Key words in Czech: *vytlačovací vyfukování, vztah zpracování-struktura-vlastnictví, objemové a místní viskoelastické vlastnosti, mikroindentace, součinitel tepelné roztažnosti*

Keywords: *extrusion blow molding, processing-structure-property relationship, bulk and local viscoelastic properties, microindentation, coefficient of thermal expansion*

Full text of the doctoral thesis is available in the Library of TBU in Zlín.

ISBN 978-80-7454-892-5

## **RESUME**

Process-dependent thermo-mechanical viscoelastic properties and the corresponding morphology of HDPE extrusion blow molded (EBM) parts were investigated. Evaluation of bulk data showed that flow direction, draw ratio, and mold temperature influence the viscoelastic behavior significantly in certain temperature ranges. Flow-induced orientations due to higher draw ratio and higher mold temperature lead to higher crystallinities. To determine the local viscoelastic properties, a new microindentation system was developed by merging indentation with dynamic mechanical analysis. The local process-structure-property relationship of EBM parts showed that the cross-sectional temperature distribution is clearly reflected by local crystallinities and local complex moduli. Additionally, a model to calculate three-dimensional anisotropic coefficients of thermal expansion as a function of the process-dependent crystallinity was developed based on an elementary volume unit cell with stacked layers of amorphous phase and crystalline lamellae. Good agreement of the predicted thermal expansion with measured ones was found up to a temperature of 70 °C.

## **RESUMÉ IN CZECH**

Práce se zabývá vztahem mezi strukturními, procesními a výslednými mechanickými vlastnostmi HDPE zpracovaného technologií vytlačovacího vyfukování. Pro určitý teplotní rozsah byla statisticky potvrzena závislost mechanických vlastností vyfukovaných prvků na směr toku, rozfukovacím poměru a teplotě formy. Orientace taveniny podpořená vyšším rozfukovacím poměrem a teplotou formy vede ke zvýšení krystalinity. Pro podchycení lokálních změn ve viskoelastických vlastnostech byla, spojením indentační metody s mechanickou dynamickou analýzou, vyvinuta nová mikro-indentanční metoda, a její relevance byla potvrzena pro vybrané polymerní materiály. Byl kvantifikován vliv rozložení teplotního pole na lokální změny ve struktuře i mechanických vlastnostech, a na základě dosažených výsledků byl sestaven model pro výpočet 3D anizotropického koeficientu teplotní roztažnosti jako funkce procesem indukované krystalizace. Modelem predikované a měřené hodnoty koeficientu teplotní roztažnosti vykazují shodu do 70 °C.

## ABSTRACT

Extrusion blow molding (EBM) is applied for more than 50 years to produce hollow plastic parts. Both demands of EBM articles and requirements for more complex geometries are continuously increasing especially in packaging, chemical and automotive industries. However, some issues concerning EBM process and process-structure-properties relationships are hardly investigated, still unclear, and not fully understood.

This thesis addresses bulk as well as local process-dependent thermo-mechanical viscoelastic properties and corresponding morphologies of high-density polyethylene (HDPE) EBM parts. For the determination of local viscoelastic properties, a new microindentation system was implemented to a conventional DMA. Additionally, a model providing anisotropic coefficients of thermal expansion (CTE) as a function of the process-dependent crystallinity was developed to predict thermal expansion and shrinkage along and perpendicular to the flow or extrusion direction, which is insufficiently considered within the EBM simulation tools until today.

Data evaluation of the process-induced storage moduli showed that the influence of the variables: flow direction, draw ratio, and the mold temperature were proven to be statistically significant, and are process-dependent quantities within certain temperature ranges. The statistically insignificant data, e.g. where storage moduli were not influenced by these variables, can be explained by relaxation processes during sample storage and increasing measuring temperatures, respectively. Flow-induced orientation, higher draw ratio and higher mold temperature lead to higher crystallinities.

A new microindentation system allowing for determination of spatially resolved local viscoelastic properties was integrated to an instrument constructed to measure viscoelastic bulk properties. The merging of indentation with dynamic mechanical analysis (DMA) for standard diamond indenters and a fine tipped cone indenter showed that the complex moduli obtained for HDPE, polybutylene terephthalate, polycarbonate, and thermoplastic polyurethane coincide well with data from literature. The x-y-stage enabled the determination of spatially resolved local viscoelastic properties on surface or inner surfaces in terms of line scans or stiffness mapping.

The local process-structure-property relationship of EBM parts showed that the cross-sectional temperature distribution is clearly reflected by local crystallinities and local complex moduli. Close to the mold wall with high cooling rates, lower values are obtained than at the inner side and the middle of cross-sections with considerable smaller cooling rates. Also, a low level of biaxiality, which increased for lower mold temperature and higher draw ratio, was found.

Furthermore, the model to calculate three dimensional anisotropic CTE based on an elementary volume unit cell (EV) with stacked layers of amorphous phase and crystalline lamellae was proposed. They represent the ultimate CTE of the EV which can be used to calculate the measured thermal expansion of parts with the aid of orientation tensors similarly as in quantifying short fiber orientation distributions.

# CONTENT

Resume .....	3
Resumé in Czech .....	3
Abstract.....	4
1 State of the Art.....	8
1.1 The process of extrusion blow molding .....	8
1.2 Polymers for extrusion blow molding .....	9
1.2.1 Crystallinity, Morphology, and Orientation.....	10
1.3 Methods to determine Crystallinity, Morphology, and Orientation.....	11
1.3.1 Crystallinity .....	11
1.3.2 Morphology .....	11
1.3.3 Orientation.....	13
1.4 Determination of thermo-mechanical and viscoelastic properties .....	13
1.4.1 Dynamic mechanical analysis .....	13
1.4.2 Indentation methods .....	14
1.5 Coefficient of Thermal Expansion (CTE) .....	16
2 Aim of the Work.....	19
3 Materials and Methods .....	22
4 Discussion of the Results .....	23
4.1 Bulk process-structure-property-relationship of extrusion blow molded parts .....	23
4.1.1 Process-dependent viscoelastic properties .....	23
4.1.2 Process-dependent crystallinity.....	25
4.2 Local process-structure-property relationship of extrusion blow molded parts .....	26
4.2.1 Local cross-sectional process-dependent crystallinity .....	26
4.2.2 Local cross-sectional process-dependent mechanical properties.....	28
4.2.3 Correlation of local crystallinities to local mechanical properties.....	32

4.2.4	Local process-dependent structural properties.....	33
4.3	Modelling of thermal expansion.....	36
5	Conclusion.....	46
6	Contribution to Science and Practice .....	47
	References .....	49
	List of Figures .....	55
	List of Tables.....	56
	Abbreviations .....	57
	Symbols .....	58
	Greek symbols.....	59
	Publications, Posters, and Presentations .....	61
	Curriculum Vitae.....	63



# 1 STATE OF THE ART

Hollow polymer products manufactured by extrusion blow molding (EBM) are used in chemical and automotive industry and consumer packaging [1]. Compared to twin sheet thermoforming, rotational molding, injection blow molding, EBM is the most important processing technology to manufacture complex hollow products and the third largest plastics consuming processing technique worldwide after injection molding and extrusion molding [2,3,4]. The first commercial EBM machines appeared in the USA in the middle of the 1930s followed by further development in Europe in the late 1940s [1,5,6,7]. Until mid of 1960s the basic knowledge of the blow molding technique was acquired. During the last decade developments in blow molding focused the increase economic efficiency and sustainability [1,7].

## 1.1 The process of extrusion blow molding

The principle of extrusion blow molding process consists of the following steps, Fig. 1 [1]:

- a) Plasticization of a thermoplastic polymer into a melt using an extruder
- b) Extrusion of a molten parison (pre-form) through a die head in an open mold
- c) Closing the mold after the parison has reached the required length and sealing the parison at both ends and inserting a blow pin into the parison
- d) Inflation by blowing air through the blow pin into the parison pressing the polymer melt against the cold walls of the mold to solidify
- e) Opening the mold, retracting the blow pin from the final part and removing the final part from the mold
- f) Trimming of the flash and finishing the part

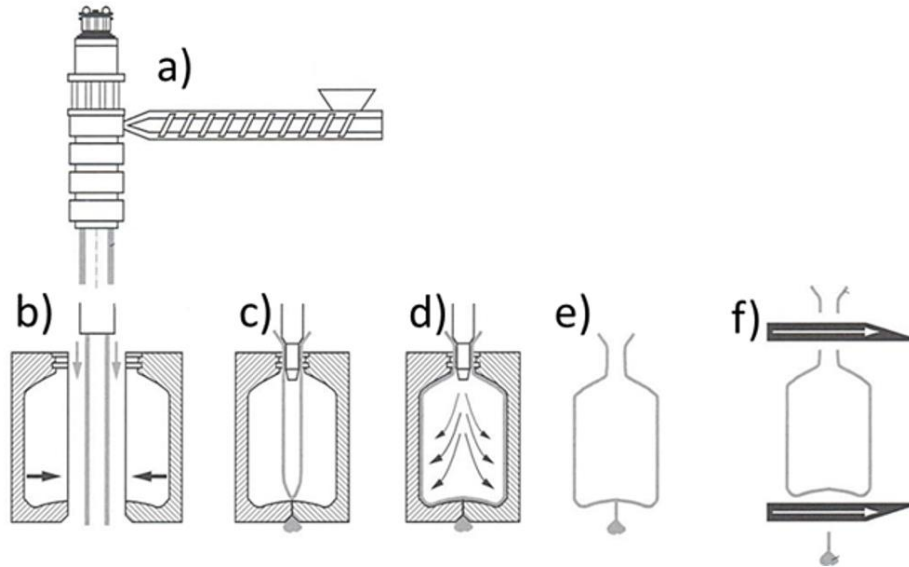


**Fig. 1 Principle of EBM [1]**

The main advantages of the EBM process are comparatively low machine and tools costs. Complex, hollow and large shapes can be molded in one piece at a high production rate [1,8]. Although EBM is successfully applied for more than 60 years now, the EBM processing still struggles with problems such as poor control of wall thickness due to die swell and sagging along the parison. With a partial wall thickness distribution system (PWDS), where a flexible deformable ring adjusts the radial die gap along the parison, and an axial wall thickness distribution system (AWDS), where the upwards or downwards movements of the mandrel adjust the parison wall thickness, this can be partly overcome [8,9]. Several EBM software simulation tools are currently available, e.g. B-Sim (Accuform), Polyflow (Ansys) and Rheoware (IMI), to calculate and predict the optimum wall thickness, temperature distribution during processing and stress distribution. However, effects related to die swell, shrinkage and warpage are not or poorly considered by them leading to inaccurate results. In particular, they do not predict mechanical properties of the final products properly [10]. Unfortunately, no extensive and comprehensive knowledge about the process-induced property-structure relation exists for the EBM process so far in contrast to injection molding [8].

## **1.2 Polymers for extrusion blow molding**

Approximately 80 % of all polymers used for EBM is high-density polyethylene (HDPE). It is commonly used in food and chemical packaging, high performance

medical and automotive applications [1,4]. Both molecular weight ( $M_w$ ) and molecular weight distribution (MWD) influence processability and final properties of polymer products. An increase of the  $M_w$  leads to more entanglements preventing melt fracture during the blowing phase, reduces the slip of segments against one to another, and leads to higher melt viscosities. A broader MWD is easier to process than a narrow MWD because the lower  $M_w$  fractions act as some kind of a lubricant and lead to parts having a lower crystallinity due to steric hindering of long chains [7,8]. Thus, the choice of processing parameters and polymer compounds allows for steering the degree of crystallinity as well as the properties of final polymer products [7].

### **1.2.1 Crystallinity, Morphology, and Orientation**

During the extrusion of the parison the macromolecules are oriented in extrusion direction. As long as the parison hangs beneath the die, these orientations have much time to relax. The blowing of the parison orients the macromolecules mainly in circumferential direction. As soon as the blown parison touches the cold mold, these orientations are frozen-in with considerably less time to relax. These orientations lead to anisotropic materials properties that may vary significantly along and perpendicular to the orientation direction. In semi-crystalline polymers, orientations in the melt ease crystallization compared to isotropic polymer melts [8].

Higher processing temperatures cause the molecules to align more readily but shortens the relaxation time due to increasing molecular motion causing the orientations to vanish. Therefore, well-combined higher temperature and faster stretching will produce an optimum orientation to meet the requirements of the final EBM part. The major challenge of the future will be to design an EBM part and to steer the EBM process in a way to produce optimal orientation and thus part properties [8].

Polymers for EBM processing require a broad processing temperature range providing enough time between extrusion and blowing of the parison without excessive sagging or solidifying too fast which causes the parison to become inflatable [1].

Polymer crystallization is a time-dependent phenomenon and depends strongly on the cooling rate during processing. High cooling rates induce many nuclei leading to a fine less ordered spherulitic structure [11,12] and a generally low degree of

crystallinity. Whereas for low cooling rates, the nuclei start the crystallization process by forming lamellae which can fan out progressively and form spherulites [11]. Due to the cooling rate gradient across the wall thickness orientations are frozen in, and the morphology changes from skin to core [13].

### 1.3 Methods to determine Crystallinity, Morphology, and Orientation

#### 1.3.1 Crystallinity

The degree of crystallinity  $X_{cr}$  can be determined by different methods such as infrared spectroscopy (IR), nuclear magnetic resonance (NMR), X-ray diffraction (XRD), and differential scanning calorimetry (DSC) whereas XRD and DSC are the most commonly used ones. From the radial intensity distribution in XRD, the integrated intensities of the crystalline peaks are related to the broader amorphous peaks to determine the crystallinity [14]. From the heat flow between sample and reference in the DSC cell, the heat of fusion  $\Delta H_m$  is determined, Fig. 2, and related to a literature value for 100 %-crystalline polymer e.g. for HDPE:  $\Delta H_m^0 = 293 \text{ J/g}$  [15,16].

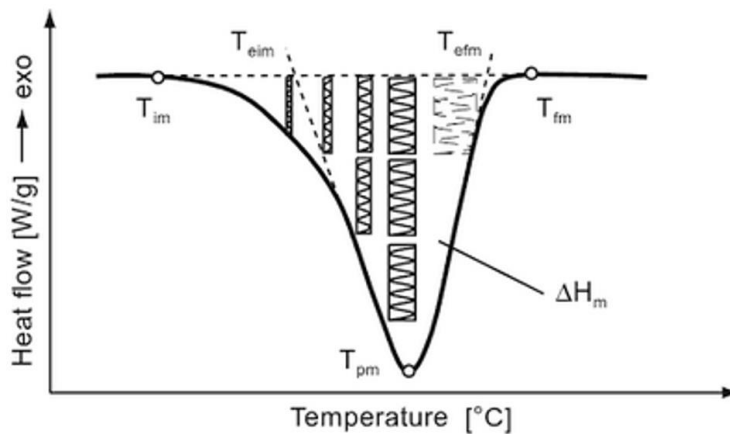


Fig. 2 Typical DSC-melting curve with crystallite thickness distribution of a semi-crystalline polymer [17]

#### 1.3.2 Morphology

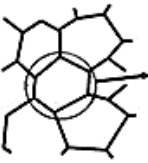




Polymers show a multiplicity of molecular and macromolecular structures ranging from 0.1 nm to 100  $\mu\text{m}$ , Table 1. Morphologies of PE samples are usually investigated by transmission light microscopy (LM) with polarized light of thin

sections, where spherulites of different shapes and sizes can be seen. Scanning electron microscopy (SEM) is used if higher resolutions of deformation structures of fracture surfaces up to 3 nm are to be investigated providing detailed information about form and orientation of the lamellae within the spherulites. Transmission electron microscopy (TEM) has an ultimate resolution to the atomic scale of 0.1 nm. TEM images provide detailed information about lamellae thickness, lamellae orientation and lateral lengths of the lamellae. Atomic force microscopy (AFM) provides further structural information such as topographic spatial details parallel and perpendicular to the sample surface. A polished AFM sample can show clear lamellar structures because of the differences between the hard lamellae and the softer amorphous areas [18]. Morphological investigations indicate the influence of processing parameters on lamellae structure and orientation [13,19].

**Table 1 Structure qualification with corresponding scale [18]**

<b>Structure qualification</b>	<b>Structures</b>	<b>Scale</b>	<b>Method</b>
Molecular level	Monomers macromolecules	0.1 nm to 10 nm	TEM/XRD/AFM
Microscopic level	Lamellae shape, size and orientation	10 nm to 1 $\mu$ m	SEM/TEM/AFM
Mesoscopic level	Spherulites shape, size and orientation	1 to 100 $\mu$ m	LM/SEM
Macroscopic level	Voids, cracks, heterogeneity	$\geq$ 0.1 mm	LM

				
Size and shape of spherulites	Interior structure of spherulites	Arrangement of lamellae	Structure of lamellae	Crystal structure, orientation

$\approx$ 100 $\mu$ m	10 $\mu$ m	1 $\mu$ m	100 nm	10 nm	1nm	0.1 nm
-----------------------	------------	-----------	--------	-------	-----	--------

Overview of structural and morphological elements of semi-crystalline polymers from nm to  $\mu$ m scale

### 1.3.3 Orientation

Birefringence, IR-fluorescence and polarized Raman spectroscopy, NMR and X-ray diffraction are used to quantify molecular orientations [19]. The standard method to quantify orientation in polymers is wide-angle X-ray diffraction (WAXD) with diffraction angles larger than  $4^\circ$ . The X-ray beam hits a sample and is diffracted generating Debye-Scherrer rings. The evaluation of the diffracted intensity along these rings contains the orientation information with respect to a certain crystallographic direction which is usually represented in pole figures. From the pole figure, the diffraction intensity distribution of the crystalline reflection has to be integrated to obtain  $\overline{\cos^2 \phi_{i,j}}$  for the calculation of the orientation factors:

$$\overline{\cos^2 \phi_{ij}} = \frac{\int_0^\pi \int_0^{2\pi} I_{hkl}(\phi_j, \alpha_j) \cos^2 \phi_j \sin \phi_j d\alpha_j d\phi_j}{\int_0^\pi \int_0^{2\pi} I_{hkl}(\phi_j, \alpha_j) \sin \phi_j d\alpha_j d\phi_j} \quad (1)$$

EBM generates orientations in all spatial directions. Several approaches for the quantification of biaxial orientation were developed [20-25] based on the description of uniaxial orientation of polymer fibers by Hermans [26-29]. The biaxial orientation functions of White and Spruiell [30] allowed for a new approach of orthorhombic lattice systems using Eq. (1).

## 1.4 Determination of thermo-mechanical and viscoelastic properties

### 1.4.1 Dynamic mechanical analysis

The dynamic mechanical analysis (DMA) allows for measuring viscoelastic complex moduli of materials as a function of temperature and frequency. Significant changes of the complex modulus indicate phase changes such glass transition, crystallization or melting. [17,31].

Usually a small sinusoidal deformation  $\varepsilon(t, \omega)$  is applied to a sample and the phase-shifted force response  $\sigma(t, \omega)$  is measured, Fig. 3.

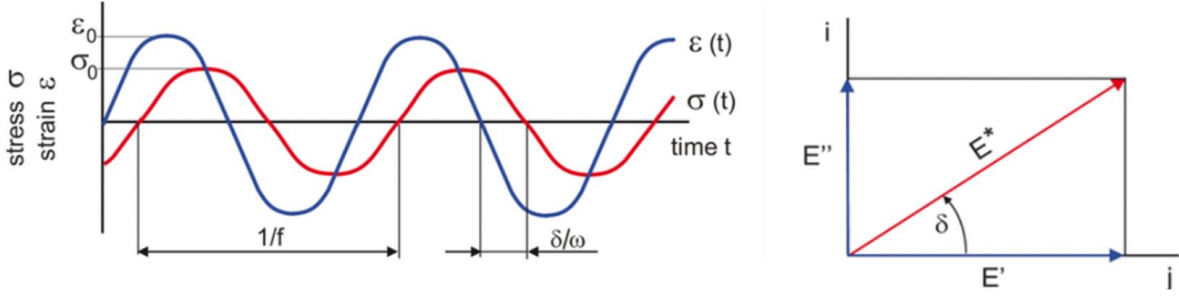


**Fig. 3 Sinusoidal input ( $\varepsilon(t, \omega)$ ) and the response signal ( $\sigma(t, \omega)$ ) with the phase angle  $\tan\delta$  (left); diagram of the modulus  $E^*$  in the complex plane (right) [32]**

The strain  $\varepsilon(\omega, t)$  is given by:

$$\varepsilon(\omega, t) = \varepsilon_0(\omega) \sin(\omega t) = \varepsilon_0(\omega) * e^{i(\omega t)} \quad (2)$$

with the strain amplitude  $\varepsilon_0(\omega)$ . The measured response stress  $\sigma(\omega, t)$  is:

$$\sigma(\omega, t) = \sigma_0(\omega)(\sin \omega t + \delta(\omega)) = \sigma_0(\omega) * e^{i(\omega t + \delta(\omega))} \quad (3)$$

with stress amplitude  $\sigma_0(\omega)$  and phase angle ( $\delta$ ). Then the complex modulus  $E^*(\omega)$  is given by:

$$E^*(\omega) = \frac{\sigma_0(\omega) * e^{i(\omega t)} * e^{i(\delta)}}{\varepsilon_0(\omega) * e^{i(\omega t)}} = \underbrace{\frac{E_0(\omega) \cos \delta(\omega)}{\text{Storage modulus } E'(\omega)}}_{\text{Storage modulus } E'(\omega)} + i \underbrace{\frac{E_0(\omega) \sin \delta(\omega)}{\text{Loss modulus } E''(\omega)}}_{\text{Loss modulus } E''(\omega)} \quad (4)$$

The real part of the complex modulus  $E^*(\omega)$  represents the storage modulus  $E'(\omega)$  which is a measure of the elastic behavior and the imaginary part of the complex modulus  $E^*(\omega)$  represents the loss modulus  $E''(\omega)$  which is a measure of the viscous behavior and lags behind by the phase angle  $\delta(\omega)$ , respectively. The ratio  $E''(\omega)/E'(\omega)$  is  $\tan\delta(\omega)$  or loss factor used as a measure for the damping behavior of a viscoelastic material. As polymer processing influences the mechanical behavior, DMA is the preferred method to determine process-induced viscoelastic behavior.

### 1.4.2 Indentation methods

Indentation methods allow for determining local mechanical properties of materials. Instrumented indentation measures force and displacement during loading and unloading which allows for the determination of e.g. indentation hardness, stiffness, elastic modulus. Oliver and Pharr [33,34] developed a method to extract Young's

modulus using the stiffness  $S$ . The contact stiffness of the sample is related to the reduced modulus  $E_r$  and the indenter contact area  $A$ :

$$S = \left( \frac{dP}{dh} \right)_{h=h_{max}}^{unload} = \frac{2}{\sqrt{\pi}} * E_r * \sqrt{A} \quad (5)$$

where the reduced modulus  $E_r$  depends on moduli and Poisson's ratios of indenter and sample, respectively. The modulus of the sample can be calculated from:

$$E_s = \frac{(1-\nu_s^2)}{2} * \frac{\sqrt{\pi}}{\sqrt{A}} * S \quad (6)$$

Modern instrumented indentation techniques such as micro-indenter, nano-indenter and atomic force microscopy (AFM) are usually operated with a three-sided pyramidal indenter, the Berkovich indenter. The indentation dependent contact area is given by

$$A = 3\sqrt{3} * h^2 * \tan^2 \theta = 24.5 * h^2 \quad (7)$$

with  $\theta = 65.27^\circ$  as the half space angle for the Berkovich tip [35].

An important issue that has to be considered during indentation is the response of the sample in terms of sinking-in or piling-up. Instrumented indentation analysis is based on sinking-in. However, if piling-up occurs, the contact depth exceeds the measured indentation depth and the calculated elastic modulus is overestimated [34,36].

A further issue is the determination of the first contact of the indenter with the sample surface. The first contact can be determined by monitoring force and indentation at a high indenter speed and a sharp rise of the force is set as the point of contact [37]. Alternatively, the first contact is given if the contact force exceeds a preset small value. Afterwards, the curve must be fitted to determine the first contact as an offset for obtaining adequate loads and displacements [35].

### **Instrumented nanoindentation**

Over the last 30 years, instrumented nano-indentation (INI) has become a routine technique to investigate mechanical properties of thin films, coatings, blends/alloys, and composites. Since INI works with lower loads and displacements, the effect of surface energies and their related adhesive forces may become relevant for the force behavior on the nanoscale [37-40]. Beside the adhesive forces friction between sample and indenter may influence the indentation measurements. A larger indenter



tip angle inhibits a higher effect of friction [41]. Furthermore, the roughness of the sample surface also influences indentation measurements.

The indentation size effect (ISE), a scale-dependent behavior as the hardness increases with decreasing penetration depths, may become relevant at penetration depths lower than 1  $\mu\text{m}$  or for spherical indenters with diameters less than 100  $\mu\text{m}$ . An apparent ISE can be caused by false sample surface preparation and/or errors in indenter area-function and instrument compliance calibration [42]. In comparison with metals, the literature on the ISE of polymers is scarce and the mechanism not well understood [43-45].

### **INI - dynamic mode**

Beside the conventional quasi-static instrumented indentation measurements, the dynamic instrumented indentation, generally called continuous stiffness measurements (CSM), allows the determination of local viscoelastic properties. Similar to the DMA, the CSM applies a small sinusoidal load  $P(t)$  at a given frequency  $\omega$  imposed on a quasi-static indentation load  $P_{static}$ . According to the determination of the complex modulus  $E^*$ , Eq. (4), and the stiffness  $S$ , Eq. (5), the time-dependent stiffness  $S(t)$  is given by

$$S(t, \omega) = \frac{P(t, \omega)}{h(t, \omega)} = \frac{2}{\sqrt{\pi}} * E^*(\omega) * \sqrt{A} \quad (8)$$

which is true for instruments with infinitive stiffness and for ideal elastic solids. To determine the real instrument stiffness, a solid instrument compliance calibration has to be performed. A further advantage of the CSM is that it provides a more accurate measurement as there is no initial surface contact problem what significantly decreases the measuring time [37,46,47].

EBM parts should exhibit an asymmetric temperature distribution across the wall thickness which should be reflected in crystallinities and local mechanical properties. INI should be able to measure Young's moduli across the part thickness [48-50].

## **1.5 Coefficient of Thermal Expansion (CTE)**

All materials change dimensions if temperature varies. As the behavior of polymers is mainly dominated by van der Waals interaction, their thermal expansion is significantly more pronounced than that of metals and ceramics. The coefficient of thermal expansion CTE is given by

$$\alpha_{measured}(T) = \frac{\Delta L(T)}{L_0} * \frac{1}{\Delta T} = \frac{\varepsilon(T)}{\Delta T} \quad (9)$$

with temperature dependent length change  $\Delta L(T)$ , initial length  $L_0$ , temperature change  $\Delta T$  and temperature induced strain  $\varepsilon(T)$  [17]. In the case of semi-crystalline polymers, thermal expansion is relatively complicated due to the lamellae structure. The behavior of thermal expansion for semi-crystalline polymers is basically governed by at least three CTE's:

1. **CTE of crystalline region – along the crystallographic c-axis ( $\alpha_{cr}^{\parallel}$ )**  
Thermal expansion is governed by strong covalent bonding forcing along the chains and weak van der Waals forces perpendicular to the chains. This leads to CTE being close to zero or even negative [51-53].

2. **CTE of crystalline region – perpendicular to the crystallographic c-axis ( $\alpha_{cr}^{\perp}$ )**

In the crystalline region the chains are denser packed than in the amorphous region. Thus, the larger van der Waals forces lead to smaller CTEs compared to  $\alpha_{am}$  [51]. CTE may differ for the crystallographic a- and b-axes due to the crystal lattice and an anisotropy in thermal expansivity is to be expected [51,52,54].

3. **CTE of amorphous region ( $\alpha_{am}$ )**

It is considered to be isotropic as long as it is kept above  $T_g$  in the molten state where the orientation of chains can relax. The CTE is given by that of the melt.

Below  $T_g$ ,  $\alpha_{am}$  approaches  $\alpha_{cr}^{\perp}$  as the binding energies become similar [52,55].

CTE's depend on processing and may differ significantly from the CTE of crystalline and amorphous phases, Table 2. This means that measured CTE  $\alpha_{measured}$  have to depend on microscopic CTE  $\alpha_{cr}^{\parallel}$ ,  $\alpha_{cr}^{\perp}$ , and  $\alpha_{am}$ , degree of crystallinity  $X_{cr}$  and process-induced orientations. Highly oriented polymers in the amorphous phase may even shrink upon heating.

**Table 2 CTE of PE and PP of crystalline phase, amorphous phase and produced parts**

<b>Polymer</b>	<b>PE-HD</b> (Backbone forms an all-trans chain configuration in the crystalline phase.)	<b>PP</b> (Backbone forms a helical chain configuration in the crystalline phase.)
$\alpha_{cr}^{\parallel}$	$-13 * 10^{-6} * K^{-1}$ [52,54,56-58]	$-10 * 10^{-6} * K^{-1}$ [58]
$\alpha_{cr}^{\perp}$	$40-130 * 10^{-6} * K^{-1}$ [52,54,57,58]	$136 * 10^{-6} * K^{-1}$ [58]
$\alpha_{am}$	$300 * 10^{-6} * K^{-1}$ [56-58,62]	$98 * 10^{-6} * K^{-1}$ [58]
$\alpha_{measured}^{injection\ molded}$	$145 * 10^{-6} * K^{-1}$ [59]	$61 * 10^{-6} * K^{-1}$ [59]
$\alpha_{measured}^{fiber}$	$-12.3 * 10^{-6} * K^{-1}$ [60,61]	$-8.7 * 10^{-6} * K^{-1}$ [58]

***Measurement of CTE using thermomechanical analysis (TMA)***

A TMA device is an instrument that allows for sensitive measuring of thermally induced length changes due to a defined temperature protocol and is therefore able to determine process-induced anisotropic thermal behavior. An important issue for precise TMA measurements in compression and penetration mode is the sample to be absolute plane parallel. This can be achieved by accurate sample preparation with e.g. a diamond annular saw under steady water cooling to avoid thermal induced property changes. For the TMA measurements in tension and 3-point bending it is essential the sample the have a consistent thickness distribution for the entire measuring length.

Furthermore, the thermal expansion can also be determined by DMA in tension mode, but with less resolution than the TMA. Although the DMA measures dynamical, with very low loads and amplitudes the influence of the measuring method on the samples' expansion is brought to a minimum and a good enough resolution can be achieved.

## 2 AIM OF THE WORK

A poor wall thickness control during EBM processing caused by e.g. die swell and parison sagging during the extrusion phase of EBM are insufficiently comprehended. Furthermore, even up to now there are not many research papers dealing with the processing-structure-property relationship of EBM in contrast to injection molding.

The chosen EBM processing parameters such as mold temperature, and draw ratio influence the structure formation process, which determines thermo-viscoelastic properties, and thus the long-term performance of any manufactured part.

The cooling conditions of the EBM process are not symmetric due to a cold mold on the outside and ambient air on the inside. Thus, all manufactured parts should exhibit an asymmetric, cross-sectional crystallinity distribution and correspondingly asymmetric cross-sectional stiffness and strength dependencies. Therefore, another focus of the PhD work addresses the determination of local crystallinities and local mechanical properties such as local stiffness over the wall thickness of a part. To achieve this goal new testing methodologies have to be developed.

The focus of this work lies in the following points:

- gaining a detailed understanding of how the chosen processing parameters affect structure formation during solidification and the final morphology of EBM parts
- correlating final morphology to the corresponding anisotropic thermo-viscoelastic properties
- developing a new model for anisotropic crystallinity dependent thermal expansion to allow for the prediction of shrinkage for an optimization of EBM parts (this model is to be implemented in FE packages developed to calculate the performance of EBM parts but the implementation is not part of this PhD work).

In the case of the mostly used polymer for EBM, polyethylene (PE), the relevant morphological quantities are molecular and lamellar orientation (investigated by X-ray diffraction (WAXD and TMA), crystallinity (by DSC) and the spherulitic superstructure (by LM and TEM). These morphological quantities have to be correlated to the thermo-viscoelastic behavior mainly determined by DMA over a wide frequency and temperature range.

The presented results are also summarized in the following publications:

- I On merging DMA and microindentation to determine local mechanical properties of polymers.**  
E. Ramakers-van Dorp, T. Haenel, F. Sturm, B. Möglinger, B. Hausnerova;  
*Polymer Testing*, 2018, Volume 68, 359-364
- II Development of an advanced dynamic microindentation system to determine local viscoelastic properties of polymers.**  
E. Ramakers-van Dorp, T. Haenel, D. Ciongwa, B. Möglinger, B. Hausnerova  
*Polymers*, 2019, Volume 11, 833-846
- III Process-dependent structural and deformation properties of extrusion blow molding parts.**  
E. Ramakers-van Dorp, C. Blume, T. Haedecke, V. Pata, D. Reith, O. Bruch,  
B. Möglinger, B. Hausnerova  
*Polymer Testing*, 2019, Volume 77, 105903
- IV Local process-dependent structural and mechanical properties of extrusion blow molded high-density polyethylene hollow parts**  
E. Ramakers-van Dorp, B. Eger, C. Raschen, M. Urbanek, B. Möglinger, B. Hausnerova  
Submitted to *Polymer Testing*, September 2019
- V Thermal expansion of semi-crystalline polymers: Anisotropic thermal strain and crystallite orientation**  
E. Ramakers-van Dorp, B. Möglinger, B. Hausnerova  
Submitted to *Polymer*, November 2019

The final long-term goal is the theoretical prediction of cross-sectional distributions of crystallinity and viscoelastic properties of EBM parts based on the chosen processing parameters. If these cross-sectional distributions are known, it is possible to calculate the bulk part behavior (internal stress states and warpage) for any given load case. Furthermore, this approach provides information where the wall thickness can be reduced to save raw materials.

A better understanding of the processing-structure-property relationship of EBM processing provided in the Thesis, Fig. 4, will lead to optimized thermo-viscoelastic performance of EBM parts and more sustainable parts due to significant reductions of polymer use and energy input as well as waste.

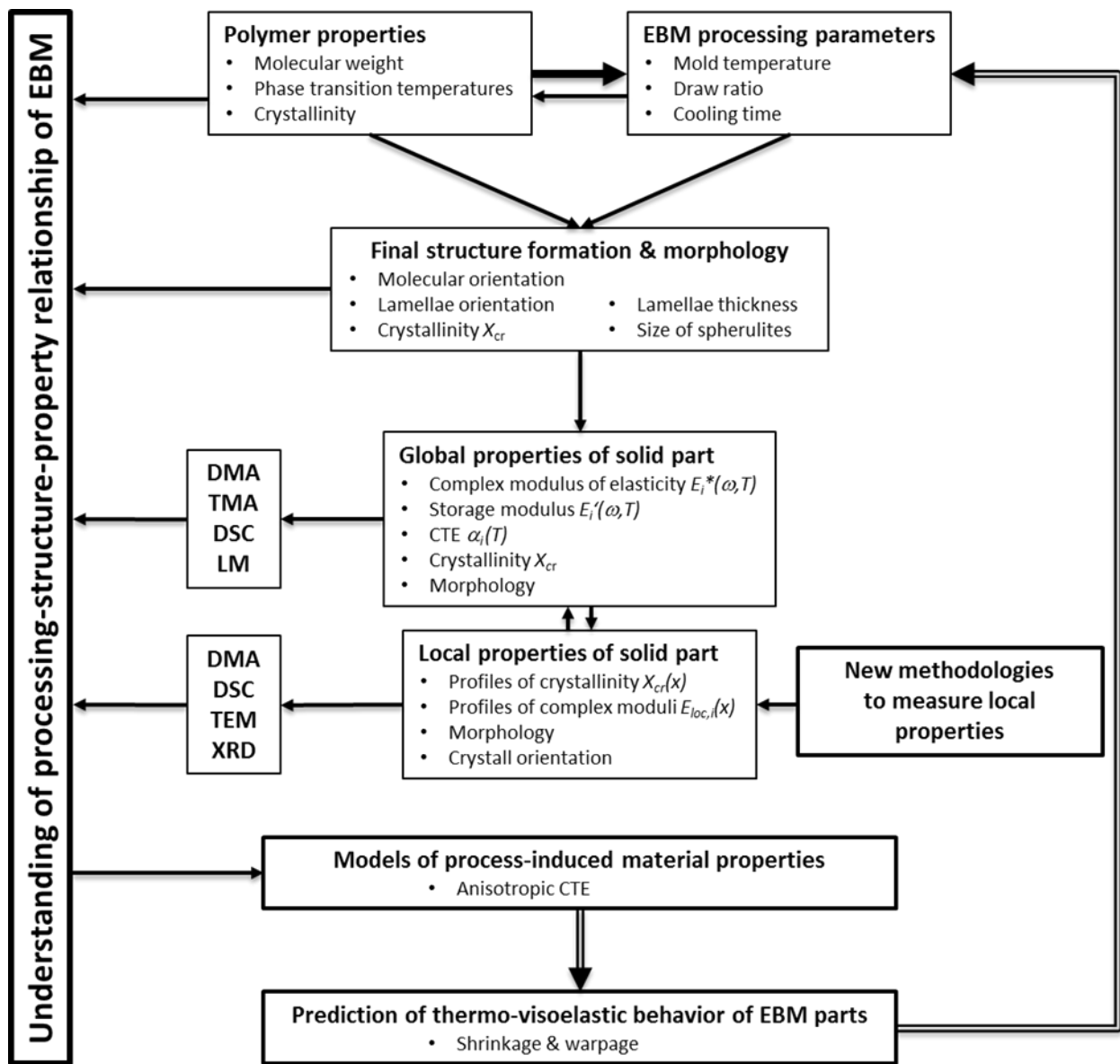


Fig. 4 Flow chart of the methodology and techniques employed in the PhD thesis

### 3 MATERIALS AND METHODS

Material used in this study was a commercial HDPE (Lupolen 4261AG, LyondellBasell) with a nominal density of 0.946 g/cm<sup>3</sup> at 23 °C and a mass flow ratio (MFR 190 °C, 21.6 kg) of 6 g/10 min [63]. For this study, hollow containers were produced on an extrusion blow molding machine BFB 2-30 T (Müller Fischer, Germany) by using a special mold that was developed in a preliminary study [64]. The containers were produced at two different mold temperatures (5 °C and 50 °C) and draw ratios (2 and 3.4).

Methods to determine the bulk and local process-dependent thermo-viscoelastic properties are listed in Table 3.

**Table 3 Measuring methods, determined quantities, instruments and standards**

<b>Method</b>	<b>Measured quantity</b>	<b>Instrument</b>	<b>Standard</b>
<b>DMA</b>	Storage modulus	Netzsch DMA 242 C 3-point bending mode	EN ISO 6721-1 [65] EN ISO 178 [66]
	3-point bending @ 1 Hz, 50 µm maximum amplitude, 5 N maximum dynamic force, 0.5 N static preload, from -40 °C up to 100 °C with 2 K/min heating rate		
<b>DSC</b>	Crystallinity	Perkin Elmer DSC 8000	EN ISO 11357-3 [67]
	-20 °C up to 180 °C with 20 K/min heating rate in a nitrogen atmosphere		
<b>TEM</b>	Lamellar structure	Jeol JEM-2100	No standard
	80-100 nm cross sections, stained with ruthenium tetroxide [68], 120-160 kV		
<b>TMA</b>	Thermal expansion	Netzsch DMA 242 C Tensile mode	EN ISO 6721-1
	Tensile @ 5 Hz, 0.5 µm maximum amplitude, 0.01 N maximum load, 0.01 N static preload, from 0 °C up to 150 °C with 5 K/min heating rate		
<b>WAXD</b>	Integrated intensity	Bruker D8 Discovery	No standard
	Pole figures: 0.1 mm collimator, CuK $\alpha$ radiation at 50 kV and 1 mA, 30 s scanning time per step, rotation: 10°-steps over 360°, tilting: 9°-steps over 80°		

## 4 DISCUSSION OF THE RESULTS

### 4.1 Bulk process-structure-property-relationship of extrusion blow molded parts

Materials structures and properties of EBM parts are influenced by processing parameters such as draw ratio and mold temperature. Their influences on storage moduli with respect to flow direction were analyzed with DMA. The crystallinities were determined by DSC. Statistical evaluation affirmed significant results.

#### 4.1.1 Process-dependent viscoelastic properties

The dendrogram shows a cluster analysis of all storage moduli, Fig. 5. Besides large similarities between 10 °C temperature differences, the cluster analysis reveals two main clusters at room temperature which means that no similarity between these clusters exist. This non-similarity can be explained by the storage conditions of the extrusion blow molded samples at room temperature between production and measurement.

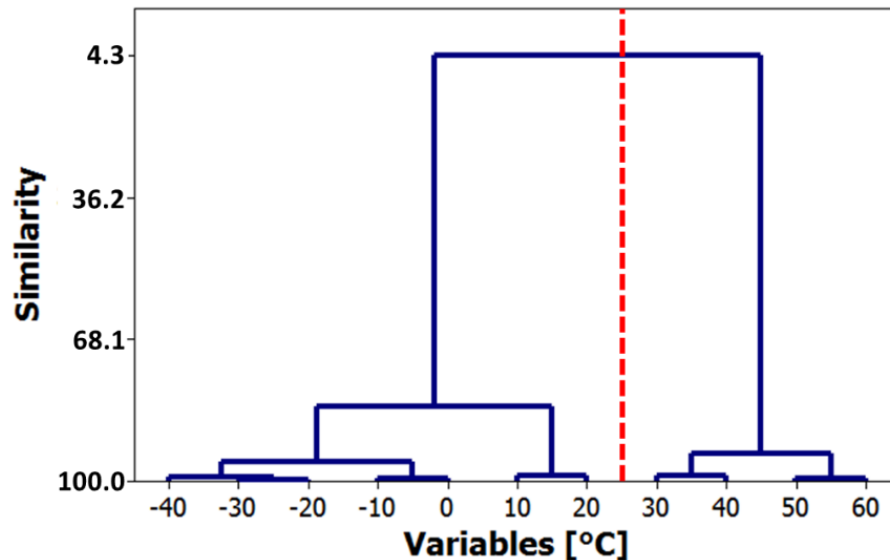
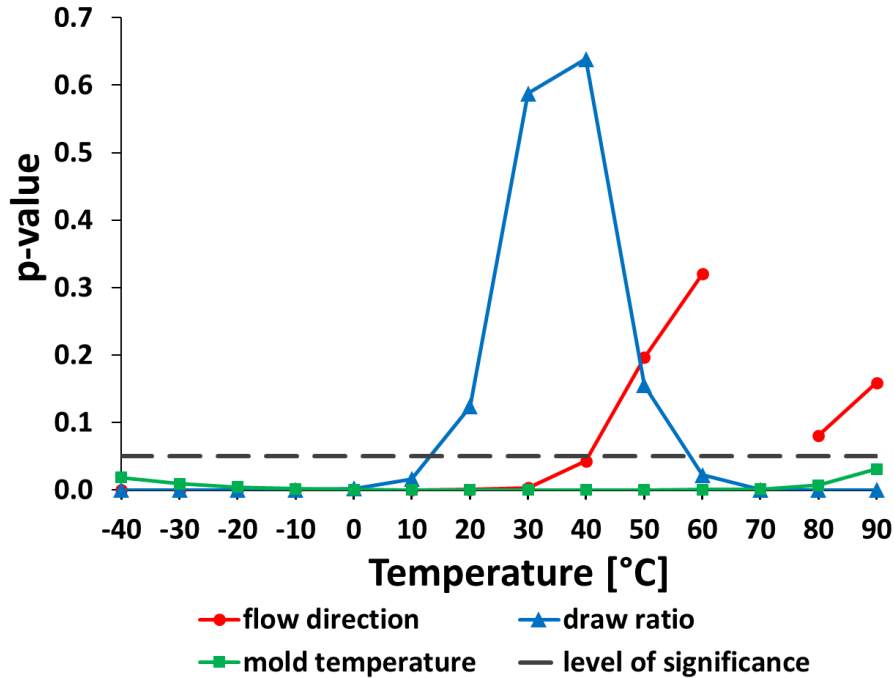


Fig. 5 Dendrogram: a cluster analysis of storage moduli (Minitab 14, Minitab Inc.)

The ANOVA ( $p$ -value = 0.05) showed that the influence of flow direction, draw ratio, and mold temperature on moduli were process-dependent for certain temperature ranges ( $p < 0.05$ ), Fig. 6. The process-independencies ( $p > 0.05$ ) can be explained by relaxation processes during sample storage around room temperature.





**Fig. 6 Statistical  $p$ -values of the variables over temperature**

Fig. 7 shows the differences in storage moduli for the flow direction parallel minus perpendicular, 3.4 draw ratio minus 2 draw ratio, and 50 °C mold temperature minus 5 °C mold temperature. For the flow direction samples measured parallel to the flow direction show higher storage modulus than the perpendicular ones. The frozen-in stretched molecules perpendicular to flow direction due to the inflation [8] cause lamellae growth in flow direction [11] increasing storage modulus. For higher temperatures the distinction between storage moduli parallel and perpendicular to the flow direction decreases due to relaxation of orientations and internal stresses.

Up to a temperature of 10 °C, for 3.4 draw ratio higher storage moduli are measured than for 2 draw ratio where the orientation caused during stretching dominates. Between 20 °C and 50 °C a cross-over is detected with negative values. Here the lower draw ratio of 2 shows higher storage moduli becoming significant above 60 °C. The insignificant and process-independent area occurs around room temperature which coincides with the sample storage temperature, Fig. 5. During sample storage and at elevated temperatures, relaxation may dissolve orientations caused by the higher draw ratio.

For the mold temperature significant positive values were obtained for the entire temperature range. A higher mold temperature reduces the cooling rate and increases

crystallinity which results in higher stiffness [69,70]. The above mentioned relaxation processes do not affect the influences of the mold temperature on modulus.

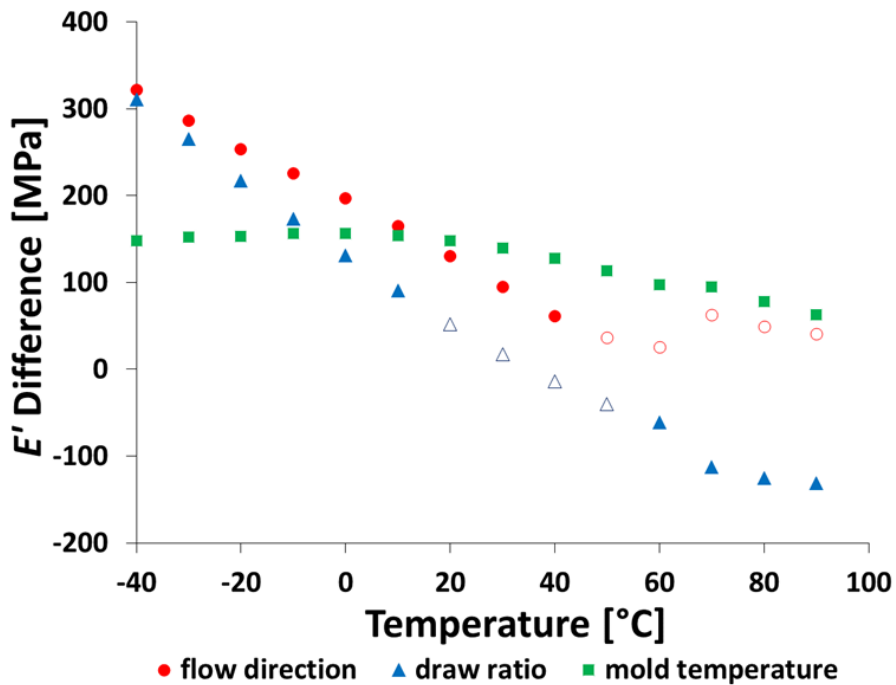


Fig. 7 Trend lines of the relative effects of statistically significant parameters over the measuring temperature

#### 4.1.2 Process-dependent crystallinity

Although there are small differences in mean crystallinities, a one tailed t-test showed that draw ratio and mold temperature have a significant influence on the crystallinity, Table 4. Higher mold temperature and draw ratio lead to higher crystallinities due to lower cooling rates and higher molecular orientation, respectively [69-73].

Table 4 Crystallinities and *p*-values for parameters mold temperature and draw ratio

Parameter		Crystallinity (%)	<i>p</i> -value
Mold temperature (°C)	5	56.3 (±0.6)	<0.001
	50	57.5 (±0.7)	
Draw ratio	2	56.2 (±0.9)	0.004
	3.4	56.9 (±1.3)	

These results of bulk properties show that the considered processing parameters influence both mechanical properties and crystallinity of EBM parts. Therefore, these process-dependent and process-independent data can be employed for more sophisticated finite element simulations to reach a more sustainable EBM production.

## **4.2 Local process-structure-property relationship of extrusion blow molded parts**

During EBM processing a temperature gradient occurs from the outer to the inner parison side due to different cooling rates because of the cold mold outside and the ambient air inside [8]. These non-isothermal cooling conditions lead to property changes across the cross section which results in different bulk and local process-dependent properties. To investigate the local process-structure-property relationship the cross-sectional changes of crystallinity were determined by DSC. As crystallinity strongly correlates to mechanical properties, local cross-sectional process-dependent complex moduli were analyzed with DMA microindentation. Furthermore, flow-induced molecular and crystallite orientation was investigated using WAXD and TEM.

### **4.2.1 Local cross-sectional process-dependent crystallinity**

Cross-sectional crystallinity of samples with two draw ratios (2 and 3.4) and two mold temperatures (5 °C and 50 °C) were determined with DSC. For all samples increasing crystallinities are found from the outer side to the inner side, Fig. 8.

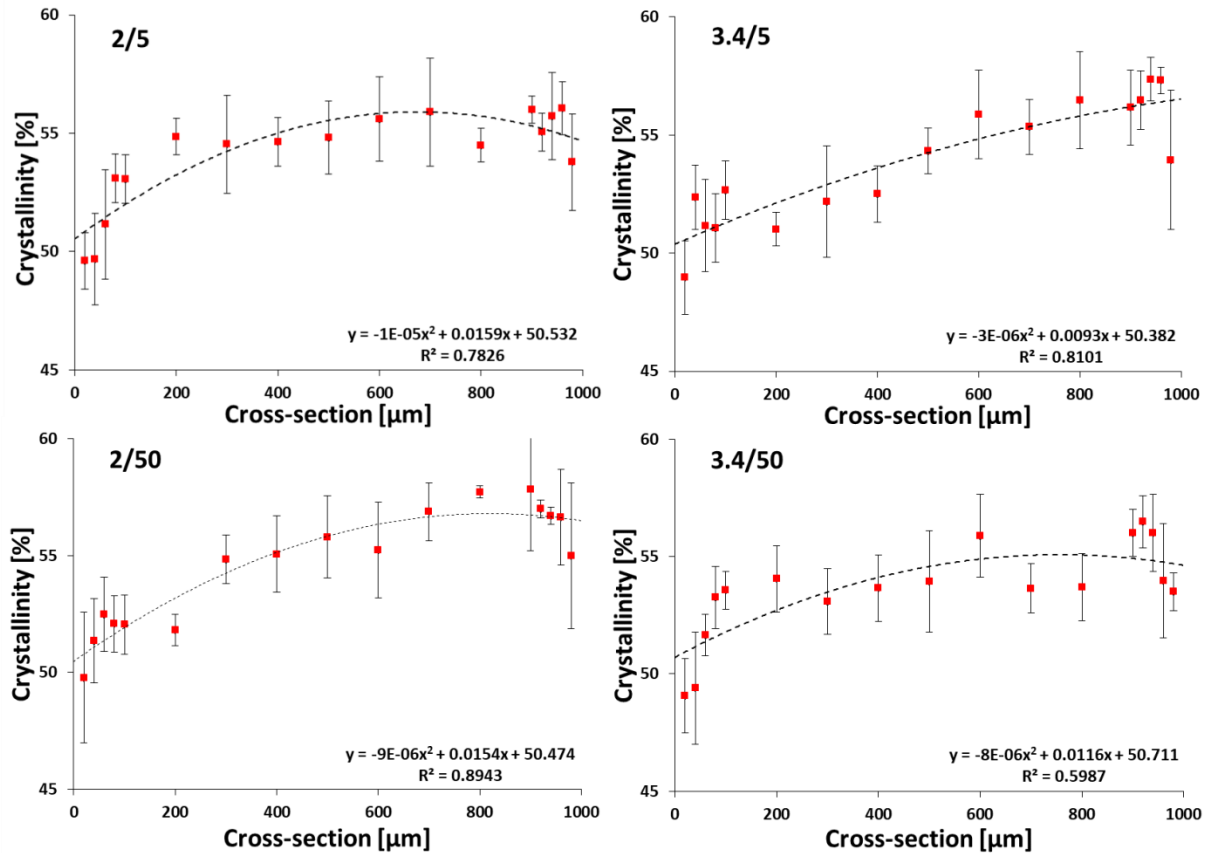


**Fig. 8 Process-dependent local cross-sectional crystallinities of the EBM part, where 0 μm represents the mold side and 1000 μm the inner side correspond to fits using a second order polynomial**

The outer and the inner side show lower crystallinities than the middle due to the cooling conditions. At the inner side lower crystallinities are found than in the middle but higher than at the mold side. This can be explained by the difference in cooling (mold and ambient air) and the effects of thermal insulation due to the low thermal conductivity of the polymer melt.

A higher draw ratio leads to slightly higher crystallinities for the samples (2/5) and (3.4/5) and vice versa for the samples (2/50) and (3.4/50). A higher mold temperature leads to slightly higher crystallinities in the case of 2 draw ratio, whereas no difference in crystallinity can be detected in the case of 3.4 draw ratio. These results indicate that higher molecular orientations due to higher draw ratio affect crystallinity only when solidification is that fast that relaxation processes cannot completely level them out. At lower mold temperature the relaxation processes have not enough time to level out the molecular orientation and crystallization benefits from it [72,73]. At higher mold temperature the relaxation processes are able to level

out the molecular orientations to a certain extent that crystallization becomes only dependent on cooling rate.

#### 4.2.2 Local cross-sectional process-dependent mechanical properties

Local mechanical material properties are usually measured with micro- or nanoindentation. Since an appropriate instrument was not available, a new measuring method was developed by merging indentation and DMA allowing for the determination of both local process-dependent mechanical and bulk properties using the same instrument.

##### *Concept and development of the DMA microindentation*

Commercially offered DMA instruments allow for measurements of viscoelastic bulk properties with respect to effects of time, temperature and frequency. To obtain access to local viscoelastic properties, a new indenter method was designed for a Netzsch DMA 242 allowing for the implementation of Berkovich, Rockwell, Vickers diamond indenters, and a fine tipped tungsten cone indenter, Fig. 9.

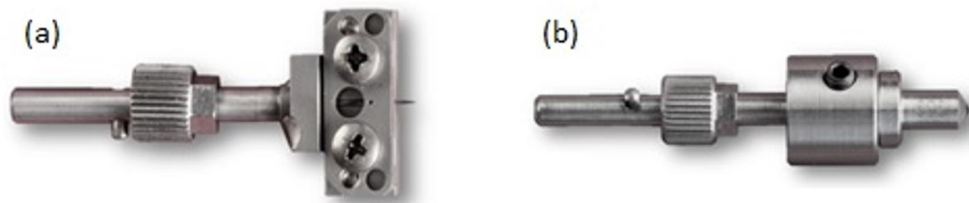


**Fig. 9 Special indenter holders for (a) tungsten needle and (b) diamond indenters**

In order to perform spatially resolved measurements, the DMA was equipped with an x-y-stage and a laser positioning system, Fig. 10.

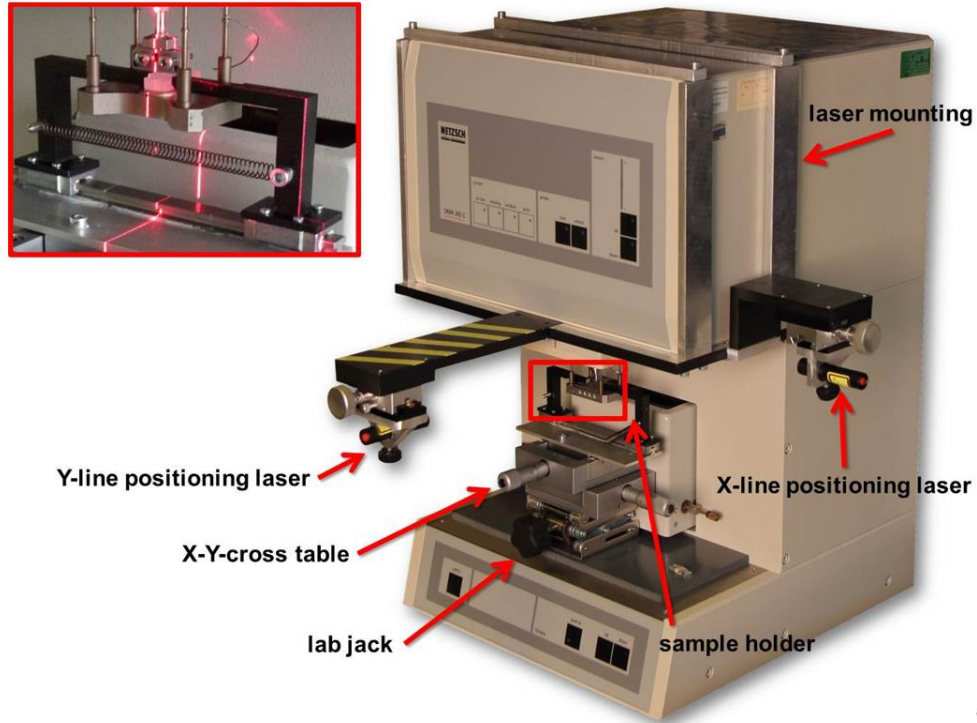


**Fig. 10 Specially developed x-y-stage with a laser positioning system for spatial resolution of microindentations**

Important issues that generally have to be considered during indentation are (a) instrument frame compliance, (b) determination of the first contact between indenter and material, (c) surface energies such as adhesive or compulsory energies between indenter and sample, (d) indentation size effect, (e) tip geometry imperfections, and (f) piling-up or sinking-in of a material (also see chapter 1.4.2).

(a) During indentation, a combined stiffness of the instrument and the sample is measured. To obtain exact results, an accurate calibration of the instrument frame compliance is essential. This ensures that only the sample response is evaluated without any influence of the instrument on the measurement [37]. The DMA 242 was therefore calibrated with a 3 mm flat punch in accordance with the manufacturers procedures.

(b) The first contact of the indenter with the sample is essential for an adequate results evaluation [35]. To obtain reliable data, the DMA microindentations were divided into 2 segments. The first segment was displacement controlled and consisted of very low amplitude and load to ensure contact between indenter and sample and to set a zero position for the following segment. The

second segment was force controlled with higher amplitude and load as the actual measurement.

- (c) The effect of surface energies and their related adhesive or compulsory forces are relevant for measurements on nanoscale [37-40]. Since the DMA microindentation works on a microscale with relatively large displacements and high loads, the surface energy effect was neglected.
- (d) The indentation size effect (ISE), where the hardness increases with decreasing penetration depths mostly caused by sample surface and/or indenter imperfections, could become relevant for penetration depths lower than 1  $\mu\text{m}$  or for spherical indenters with radii less than 100  $\mu\text{m}$  [42]. This effect was not considered as the DMA microindentation works with larger displacements.
- (e) Indentation data evaluation according to Oliver and Pharr [33,34] is based on concise axisymmetric indenter geometry. Modern indentation instruments provide a computational correction after an accurate tip calibration for further data evaluation. Since the software of the DMA 242 does not allow this computational correction, the indenter geometries were evaluated optically with a calibrated LM.
- (f) Indentation analysis is based on the elastic contact theory assuming sinking-in of the sample. Piling-up of the sample during indentation however, causes the calculation of the elastic modulus to be overestimated [35,46,74]. Since the effect of piling-up on this overestimation becomes smaller at high penetration depths [74], and there is still standard evaluation procedure, piling-up or sinking-in was not regarded within the data evaluation of the DMA microindentation.

### ***Data evaluation of DMA microindentation measurements***

The evaluation of the indentation measurements is based on the Oliver & Pharr concept [33,34] and the complex modulus  $E^*(\omega)$  was calculated with Eq. (6). The effective indentation area for the different indenter geometries can be determined using Table 5.

**Table 5 Contact areas (projected area) of the used indenter geometries**

<b>Indenter</b>	<b>Geometry</b>	<b>Contact area <math>A</math> (mm<sup>2</sup>)</b>	
<b>Berkovich</b>	angle $\alpha=65.27^\circ$	$3 * \sqrt{3} * \tan^2(\alpha) * h^2$	$24.494 * h^2$
<b>Rockwell</b>	radius $R=200 \mu\text{m}$	$\pi * 2 * R * h^2$	$1.257 * h^2$
<b>Vickers</b>	angle $\alpha=68^\circ$	$4 * \tan^2(\alpha)h^2$	$24.504 * h^2$
<b>Cone</b>	angle $\alpha=14^\circ$	$\pi * \tan^2 \alpha * h^2$	$0.195 * h^2$

The DMA analysis software, FOURIER-analyses the response signal of the sample but uses only the intensity at measuring frequency  $\omega$  for data evaluation purposes. A non-sinusoidal response signal results in pronounced intensities at higher order frequencies. Their effects may be neglected as long as their intensities do not exceed 10 % of the intensity at measuring frequency. All three diamond and the 1.0mm diameter tungsten cone indenter showed a sinusoidal response signal with less than 10 % overtones of the first order frequencies.

The complex local moduli measured with DMA microindentation on various polymers mainly correspond to complex bulk moduli measured with 3-point bending and literature values [75,76] taken from tensile tests, Table 6. Differences in the results can be explained by local inhomogeneities e.g. caused by processing.

**Table 6 Comparison of complex moduli (MPa) of the investigated polymers determined with the 4 indenter geometries, three-point bending, and Young's moduli from literature [75,76]**

<b>Polymer</b>	<b>Berkovich</b>	<b>Rockwell</b>	<b>Vickers</b>	<b>Cone</b>	<b>3-point</b>	<b>Literature</b>
<b>PBT</b>	1737±358	1821±78	1919±353	2890±378	2787±84	2500-2800
<b>PC</b>	1957±317	2142±351	2289±156	2726±386	2380±19	2200-2600
<b>PP</b>	1425±49	1394±133	1449±230	-	1716±2	1300-1800
<b>HDPE</b>	1929±302	1553±75	1381±339	1053±175	1565±33	600-1500
<b>TPU</b>	26±3	24±3	24±2	38±2	73±3	20-400

The reproducibility of complex moduli using the tungsten cone indenter was checked on unannealed and annealed PC plates with  $(3217 \pm 729)$  MPa and  $(2402 \pm 253)$  MPa, respectively. The higher value for the unannealed PC can be explained by internal stresses and molecular orientation caused by processing which could relax during annealing leading to a lower complex modulus with less scatter. In order to spatially resolve material surface properties DMA microindentations were



performed on the cross-section surface of the narrow middle part of unannealed injection molded HDPE tensile bar, Fig. 11.

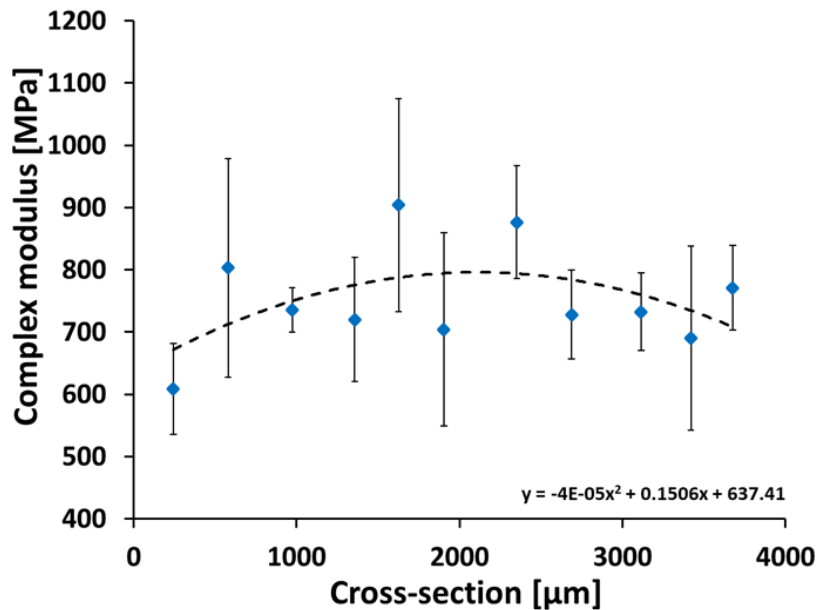


**Fig. 11 Measured complex moduli along the cross sectional area of an unannealed HDPE tensile test bar (dots) with second order polynomial fit as trend line (dashed line)**

Close to the edges of the test bar, the complex moduli exhibit lower values than in the middle. Due to fast cooling rates close to the mold, fewer crystallites were formed near the edges leading to lower complex moduli. In the center of the cross-section, slower cooling rates gave more time to crystallization leading to higher crystallinities and higher complex moduli.

The sensitivity and the reproducibility of DMA microindentation data generated by the three standard diamond indenters and the fine tipped tungsten cone indenter allow for quantitative distinguishing small differences of mechanical properties. Thus, DMA microindentation is a suitable method to resolve viscoelastic material properties spatial on a local level.

#### **4.2.3 Correlation of local crystallinities to local mechanical properties**

Spatially resolved microindentation measurements along the cross-sectional surface of EBM parts processed with mold temperatures of 5 °C and 50 °C and draw ratios of 2 and 3.4 are compared to the cross-sectional crystallinities in Fig. 12 showing three facts:

- Although the mean crystallinities are very similar it is clearly seen that a lower mold temperature leads to higher complex moduli compared to the higher mold temperature. This clearly indicates that frozen-in orientations and internal stresses also affect the complex moduli.
- The draw ratio hardly influences the complex moduli.
- Crystallinities and complex moduli close to the mold side were lower than those to the inner side and the middle of the cross-section.

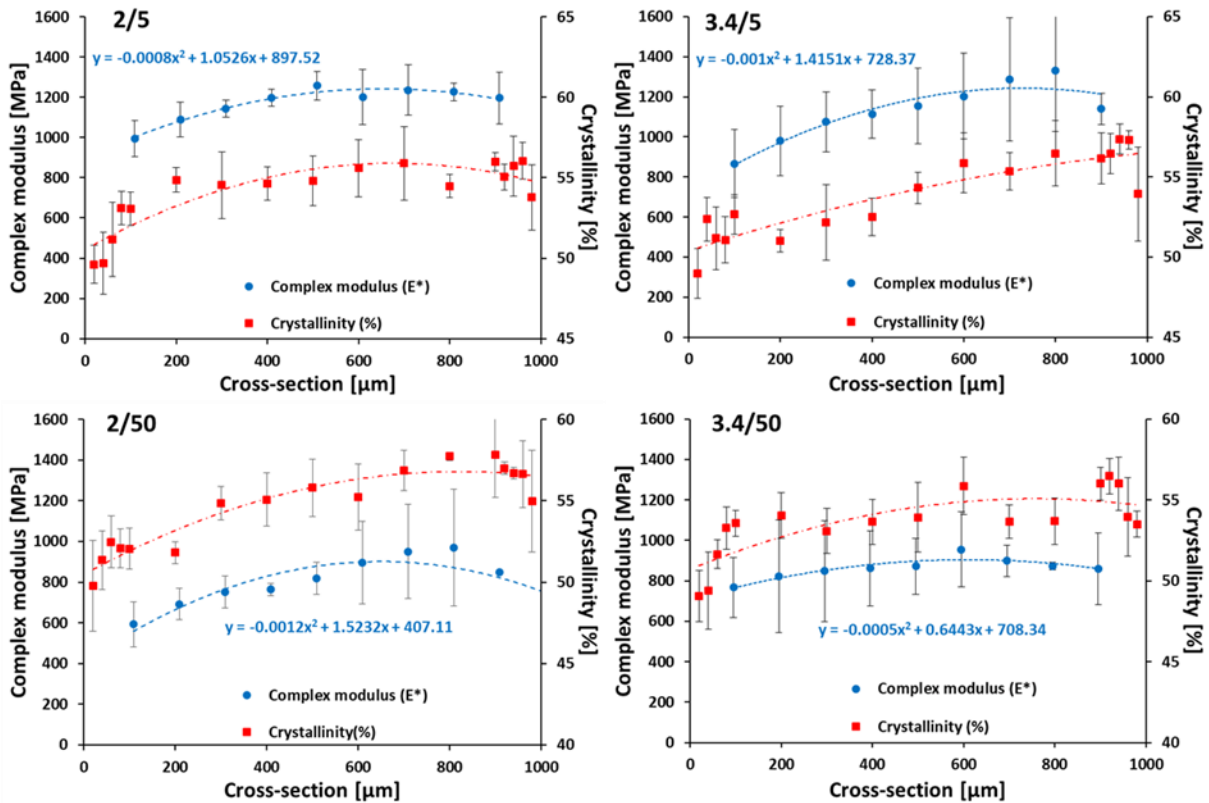


**Fig. 12** Effects of mold temperature and draw ratio on local crystallinities and complex moduli along the cross-section of the EBM part, second order polynomial fits are displayed as trend lines

#### 4.2.4 Local process-dependent structural properties

Pole figures for the a- and b-axis were measured with WAXD. A comparison of the pole figures for the a-axis of sample (2/50) and sample (3.4/5) at the mold side for which the orientation should be extreme is shown in Fig. 13. The blue ellipses in both pole figures indicate that the a-axis is similarly randomly distributed for both samples in the normal and transverse (ND-TD)-plane being perpendicular to the

MD-plane. Furthermore, the circular pattern, the red circles, indicates also random and low orientation of a-axis around the TD-plane for both samples.

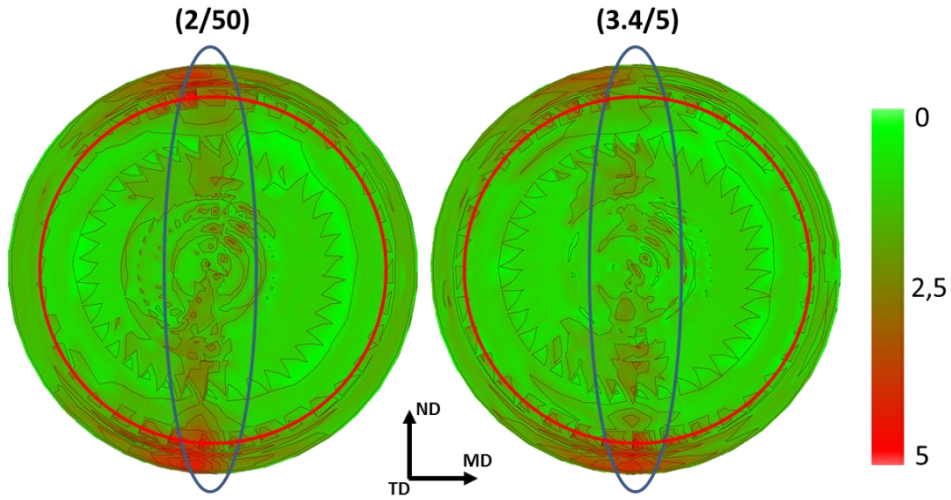


**Fig. 13 Pole figures for a-axis for sample (2/50), left, and sample (3.4/5), right**

If there is only a small preferential orientation, the orientation factors for all three axes were calculated from the pole figures using (Eq. (1)). The orientation factors indicate for all samples some kind of biaxiality,

$$f_{1a}^B \approx f_{2a}^B; \quad (10)$$

$$f_{1b}^B \approx f_{2b}^B; \quad (11)$$

$$f_{1c}^B \approx f_{2c}^B. \quad (12)$$

Since the c-axis coincides with the backbone direction of the polymer chain, these orientation factors are plotted in a White-Spruiell isosceles triangle diagram, Fig. 14. Generally, all samples show a biaxial orientation of the c-axis and are slightly oriented towards TD. The sample (3.4/5) shows more tendency towards biaxiality than the sample (2/5). Orientation in TD is caused by inflation whereas orientation in MD is caused by gravity. The only slight orientation towards TD can be explained by the fact that process-induced orientations are able to relax as long as the melt did not solidify [77].

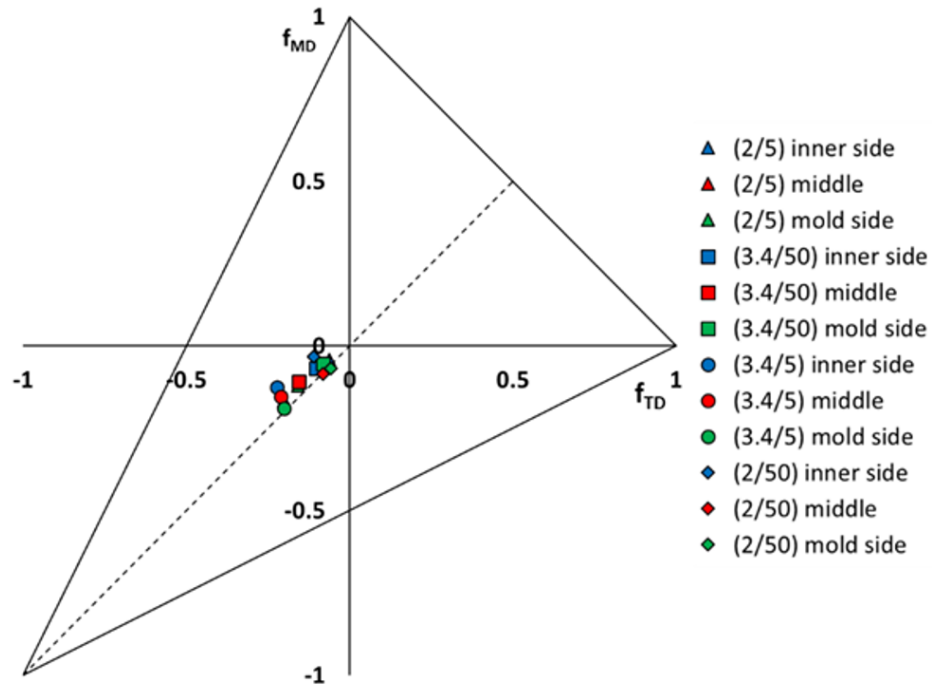


**Fig. 14 White-Spruiell isosceles triangle of c-axis of orientation factors derived from X-ray diffraction, the dashed line represents biaxial orientation**

Fig. 15 shows transmission electron micrographs for sample (3.4/5) close to mold side and inner side and both in MD and TD direction in which lamellar orientations should be most developed. However, the lamellae in all micrographs are randomly oriented showing no preferential lamellae orientation parallel or perpendicular to MD or TD. In Fig. 15(a) small spherulites are visible even close to the cold mold side as circular pattern this is consistent with isotropy and low levels of biaxiality. As the orientation factor triangle, Fig. 14, showed no clear uniaxial orientation in MD or TD as well no shish-kebab structures or other preferential lamellar orientations can be confirmed.

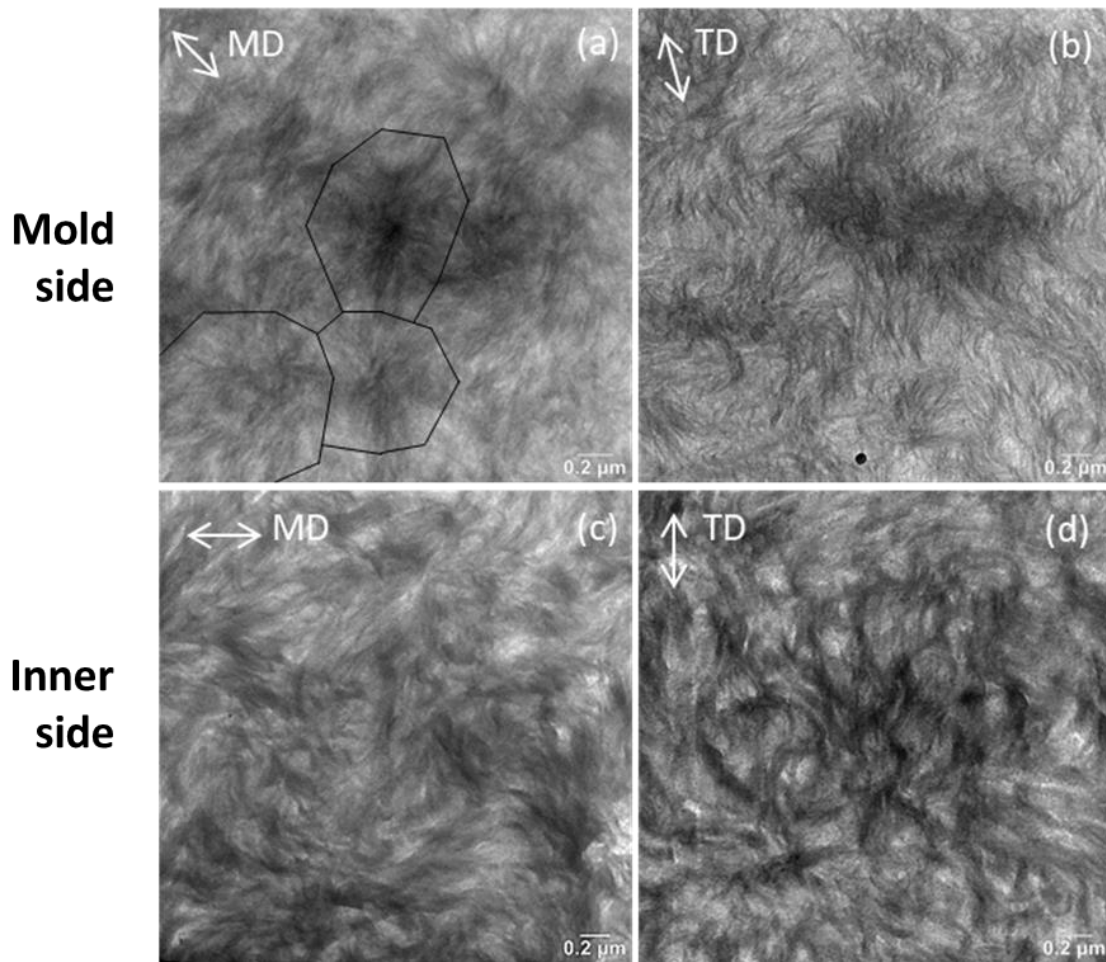


**Fig. 15** Transmission electron micrographs of sample (3.4/5), (a) parallel to MD close to the mold side, (b) parallel to TD close to the mold side, (c) parallel to MD close to the inner side, (d) parallel to TD close to the inner side

These investigations revealed an orientation of the c-axis with a low level of biaxiality having a slight tendency towards the TD which is more pronounced at low mold temperature and high draw ratio. The low level of biaxiality was supported by transmission electron micrographs showing no preferential lamellae orientation.

### 4.3 Modelling of thermal expansion

An important issue not sufficiently considered by EBM simulation software is shrinkage and warpage which is linked to thermal expansion. Therefore, a new model to calculate thermal expansion of semi-crystalline polymers was developed.

Most semi-crystalline polymers crystallize in a lamellae structure consisting of stacked amorphous and crystalline layers represented in an elementary volume unit

cell (EV), Fig. 16, given by width  $b_0$  in x-direction, thickness  $c_0$  in y-direction and height  $h_0$  in z-direction. The height of the crystalline lamellae is given by  $h_{0,cr}$ .

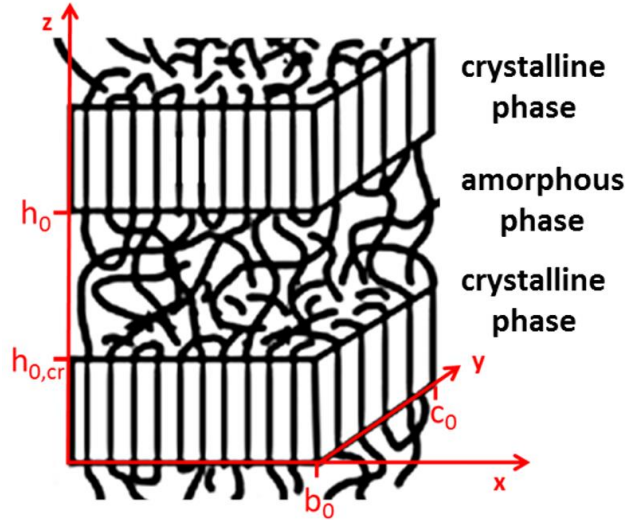


**Fig. 16 Sketch of the elementary volume unit cell (EV) for semi-crystalline polymers**

The properties of crystalline and amorphous phase differ significantly, Table 7 [52-62,78-82]. Consequently, the thermal expansion behavior of the EV has to be anisotropic.

**Table 7 Coefficient of Thermal Expansions CTE and Young's moduli of crystalline and amorphous phase of PE taken from literature [52-62,78-82]**

Property	Variable	Value
CTE perpendicular to crystal chain axis in x-direction	$\alpha_{cr,x}^{\perp}$	$100 \cdot 10^{-6} \cdot K^{-1}$
CTE perpendicular to crystal chain axis in y-direction	$\alpha_{cr,y}^{\perp}$	$60 \cdot 10^{-6} \cdot K^{-1}$
CTE along crystal chain axis in z-direction	$\alpha_{cr,z}^{\parallel}$	$-12 \cdot 10^{-6} \cdot K^{-1}$
CTE amorphous phase in x-, y- and z-direction	$\alpha_{am,x}, \alpha_{am,y}, \alpha_{am,z}$	$300 \cdot 10^{-6} \cdot K^{-1}$
Young's modulus perpendicular to crystal chain axis in x- and y-direction	$E_{cr,x,y}^{\perp}$	3,500 MPa
Young's modulus along crystal chain axis in z-direction	$E_{cr,z}^{\parallel}$	300,000 MPa
Young's modulus of amorphous phase in x-, y- and z-direction	$E_{am,x}, E_{am,y}, E_{am,z}$	10 MPa



The thermal expansion mainly takes place perpendicular to the lamellar plane in z-direction, because the volume change due to temperature of the amorphous phase is larger than for the crystalline phase:  $\alpha_{am} \gg \alpha_{cr}^\perp \gg \alpha_{cr}^\parallel$ , which constraints thermal expansion of the amorphous phase in the lamellar plane.

This behavior is shown in Fig. 17 which illustrates the establishment of anisotropic thermal expansion from initially free expansion and to anisotropic expansion by adjusting equilibrium with tensile and compression forces in x- and y-direction to calculate the ultimate CTE  $\alpha_x$ ,  $\alpha_y$ , and  $\alpha_{||}^{cr}$  of the EV.

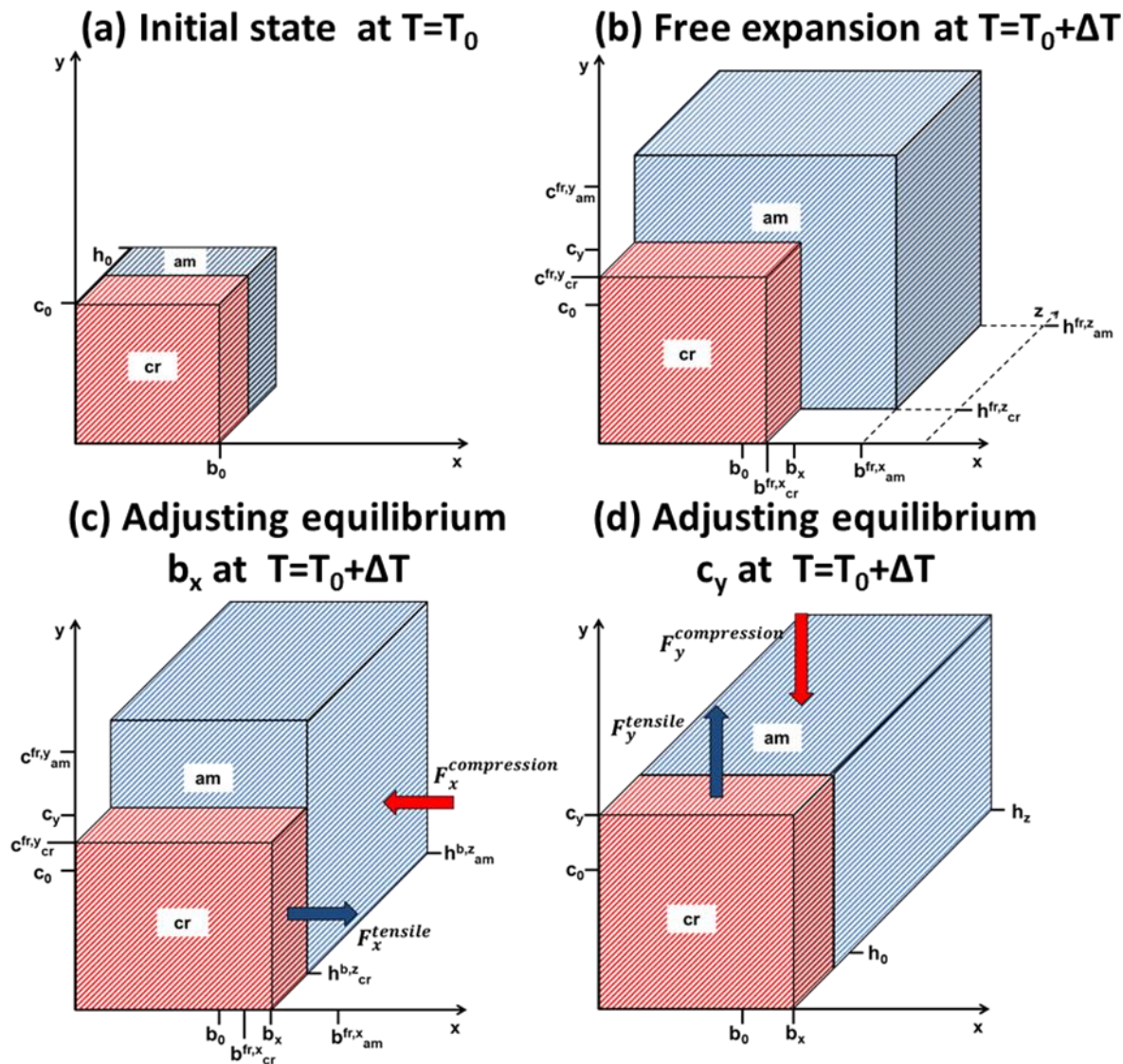


Fig. 17 The 4 stages of modelling thermal expansion to calculate the ultimate anisotropic coefficients of thermal expansion (CTE) in x-, y- and z-direction

The modelling of the EV provides the following normalized width, thickness and height:

$$\frac{b_x(T)}{b_0} = (1 + \alpha_{cr,x}^\perp \Delta T) \frac{x_{cr} - (1 - x_{cr}) \frac{(1 + \alpha_{am,z} \Delta T) (1 + \alpha_{am,y} \Delta T) E_{am,x}(T)}{(1 + \alpha_{cr,z}^\parallel \Delta T) (1 + \alpha_{cr,y}^\perp \Delta T) E_{cr,x}^\perp(T)}}{x_{cr} - (1 - x_{cr}) \frac{(1 + \alpha_{am,z} \Delta T) (1 + \alpha_{cr,x}^\perp \Delta T) (1 + \alpha_{am,y} \Delta T) E_{am,x}(T)}{(1 + \alpha_{cr,z}^\parallel \Delta T) (1 + \alpha_y \Delta T) (1 + \alpha_{am,x} \Delta T) E_{cr,x}^\perp(T)}} \quad (13)$$

$$\frac{c_y(T)}{c_0} = (1 + \alpha_{cr,y}^\perp \Delta T) \frac{\left( x_{cr}^2 - x_{cr} (1 - x_{cr}) \frac{(1 + \alpha_{am,y} \Delta T) (1 + \alpha_{am,z} \Delta T) \left( \frac{E_{am,x}(T)}{E_{cr,x}^\perp(T)} + \frac{(1 + \alpha_{cr,y}^\perp \Delta T) (1 + \alpha_{am,x} \Delta T) E_{am,y}(T)}{(1 + \alpha_{cr,x}^\perp \Delta T) (1 + \alpha_{am,y} \Delta T) E_{cr,y}^\perp(T)} \right)}{(1 + \alpha_{cr,y}^\perp \Delta T) (1 + \alpha_{cr,z}^\parallel \Delta T)^2} E_{am,x}(T) E_{am,y}(T) \right.}{\left. + (1 - x_{cr})^2 \frac{(1 + \alpha_{am,y} \Delta T) (1 + \alpha_{am,z} \Delta T)^2 E_{am,x}(T) E_{am,y}(T)}{(1 + \alpha_{cr,y}^\perp \Delta T) (1 + \alpha_{cr,z}^\parallel \Delta T)^2} E_{cr,x}^\perp(T) E_{cr,y}^\perp(T) \right)}{\left( x_{cr}^2 - x_{cr} (1 - x_{cr}) \frac{(1 + \alpha_{am,z} \Delta T) \left( \frac{(1 + \alpha_{am,y} \Delta T) E_{am,x}(T)}{(1 + \alpha_{cr,y}^\perp \Delta T) E_{cr,x}^\perp(T)} + \frac{(1 + \alpha_{cr,y}^\perp \Delta T) (1 + \alpha_{am,x} \Delta T) E_{am,y}(T)}{(1 + \alpha_{cr,x}^\perp \Delta T) (1 + \alpha_{am,y} \Delta T) E_{cr,y}^\perp(T)} \right)}{(1 + \alpha_{cr,z}^\parallel \Delta T)} \right.}{\left. + (1 - x_{cr})^2 \frac{(1 + \alpha_{am,z} \Delta T)^2 E_{am,x}(T) E_{am,y}(T)}{(1 + \alpha_{cr,z}^\parallel \Delta T)^2} E_{cr,x}^\perp(T) E_{cr,y}^\perp(T) \right)} \quad (14)$$

$$\frac{h_z(T)}{h_0} = x_{cr} (1 + \alpha_{cr,z}^\parallel \Delta T) \left( 1 - \frac{E_{cr,y}^\perp}{E_{cr,z}^\parallel} \frac{c_y(T) - c_{cr}^{fr,y}(T)}{c_{cr}^{fr,y}(T)} \right) \left( 1 - \frac{E_{cr,x}^\perp}{E_{cr,z}^\parallel} \frac{b_y(T) - b_{cr}^{fr,x}(T)}{b_{cr}^{fr,x}(T)} \right) + (1 - x_{cr}) (1 + \alpha_{am,z} \Delta T) \frac{c_{am}^{fr,y}(T)}{c_y(T)} \frac{b_{am}^{fr,x}(T)}{b_x(T)} \quad (15)$$

With them the ultimate CTE in x-, y-, and z direction can be calculated as follows:

$$\alpha_x(T) = \frac{1}{b_0} \frac{b_x(T) - b_0}{\Delta T} = \frac{1}{\Delta T} \left( \frac{b_x(T)}{b_0} - 1 \right) \quad (16)$$

$$\alpha_y(T) = \frac{1}{c_0} \frac{c_y(T) - c_0}{\Delta T} = \frac{1}{\Delta T} \left( \frac{c_y(T)}{c_0} - 1 \right) \quad (17)$$

$$\alpha_z(T) = \frac{1}{h_0} \frac{h_z(T) - h_0}{\Delta T} = \frac{1}{\Delta T} \left( \frac{h_z(T)}{h_0} - 1 \right) \quad (18)$$



Introducing CTE and Young's moduli of crystalline and amorphous phases of PE from Table 7 to Eq. (16), (17) and (18) allows for calculating the ultimate anisotropic CTE in x-, y- and z-direction as function of the crystallinity, Fig. 18.

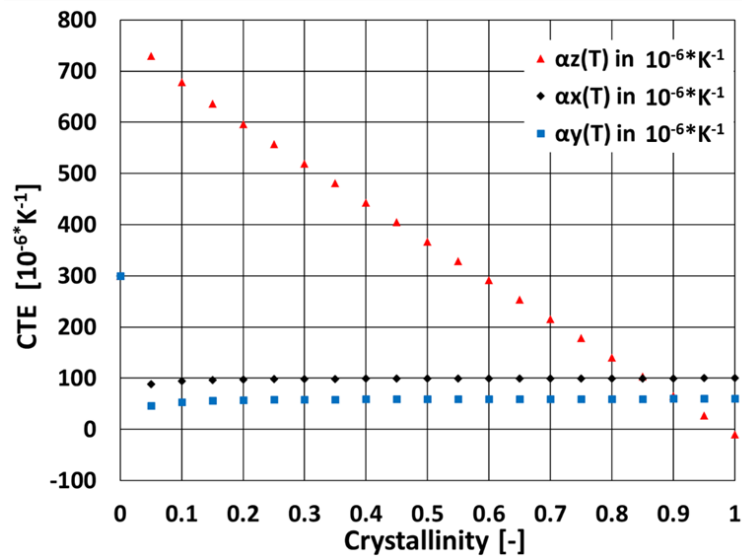


**Fig. 18 Calculation of the ultimate anisotropic CTE's as function of the crystallinity**

As expected the ultimate CTE in z-direction (along the polymer backbone of crystalline phase) strongly depends on crystallinity in contrast to the ultimate CTE in x- and y-direction. Because of the fact that the moduli of the crystalline phase exceed the moduli of the amorphous phase at least by 2 or 3 orders of magnitude thermal expansion in x- and y-direction is kept small and constant except for  $X_{cr}=0$ . Checking the boundaries shows that the model yields reasonable ultimate CTE:

- the ultimate CTE are  $300 \cdot 10^{-6} \text{K}^{-1}$  for a 100 % amorphous PE in all directions, and
- it reproduces the CTE of the crystalline phase in x-, y- and z-direction for a 100 % crystalline PE as ultimate CTE.

The thermal expansion of the EBM parts parallel to extrusion direction is lower than perpendicular to the extrusion direction (MD), Fig. 19.

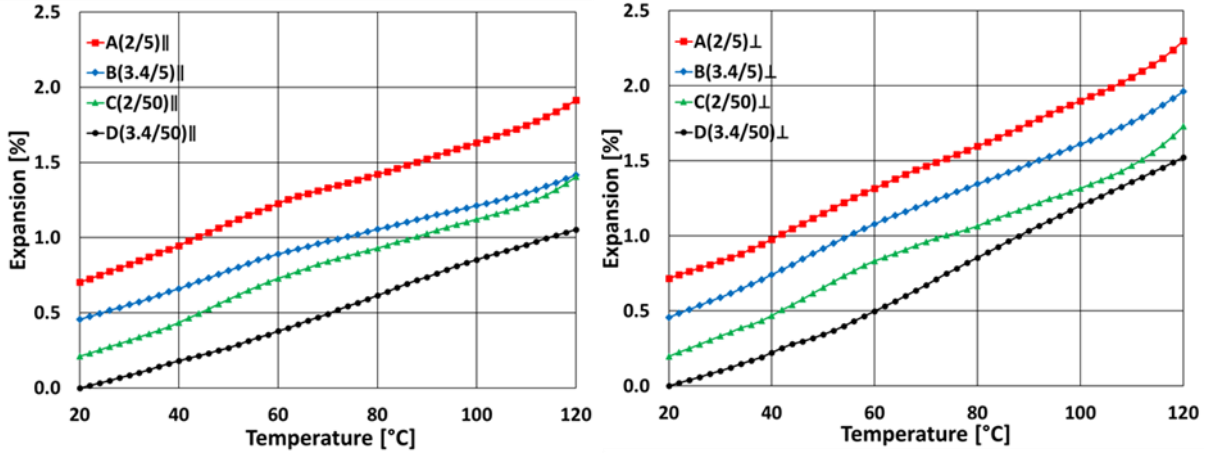


**Fig. 19 Measured thermal expansion parallel (||), left, and perpendicular ( $\perp$ ), right, to the extrusion direction (the curves A, B, and C are vertically shifted by a constant value of 0.75 %, 0.5 %, and 0.25 %, respectively, for clarity reasons)**

Due to the EBM processing the molecules were oriented in TD by stretching which causes the lamellae to grow parallel to MD. Having the EV in mind, Fig. 16, one expects a higher thermal expansion in TD (model z-direction) as the amorphous phase can expand more, and the expansion is hindered by the connected crystalline regions.

Crystallinity decreases due to partial melting when approaching the melting temperature. This has to be considered for modelling. The crystallinity of all samples decreases from approximately 55 % at room temperature to approximately 40 % at 120 °C, Fig. 20 (a). In the temperature range from 20 °C to 100 °C the samples having the higher draw ratio (3.4) show slightly higher crystallinities than the samples having the lower draw ratio (2) which can be explained by a higher molecular orientation due to higher draw ratio.

To introduce the temperature dependent crystallinity to Eq. (13), (14) and (15), the crystallinity curves were fitted using the function with the initial crystallinity  $X_{cr,0}$ , the fitting parameters  $k$  and  $n$ , the pole temperature  $T_{pole}$ .

$$X_{cr}(T) = X_{cr,0} \left( 1 - \frac{k}{\left( 1 - \frac{T}{T_{pole}} \right)^n} \right) \quad (19)$$

Fig. 20 (b) shows that Eq. (19) fits nicely the measured data.

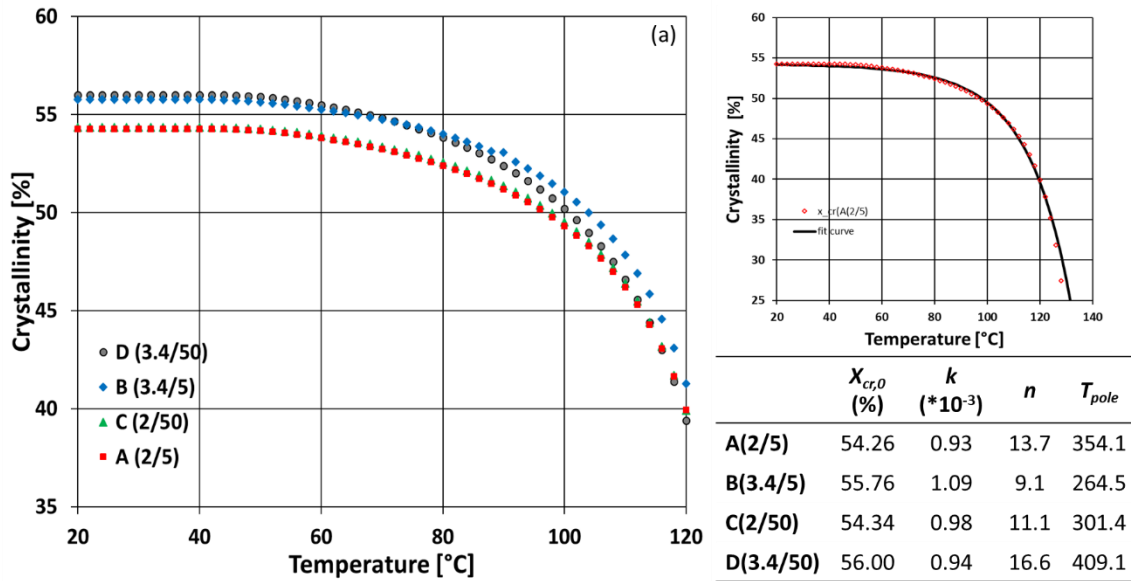


Fig. 20 (a) Temperature dependent crystallinities as a function of temperature for the EBMs, (b) fitted partial melting, (c) resulting fit parameters for modeling of CTE

The insertion of the fitting parameters in the equations of the anisotropic ultimate CTE (Eq. (13), (14), and (15)) shows that the thermal expansions of sample A (2/5) lie between the ultimate thermal expansions in x-, y-, and z-direction, Fig. 21.

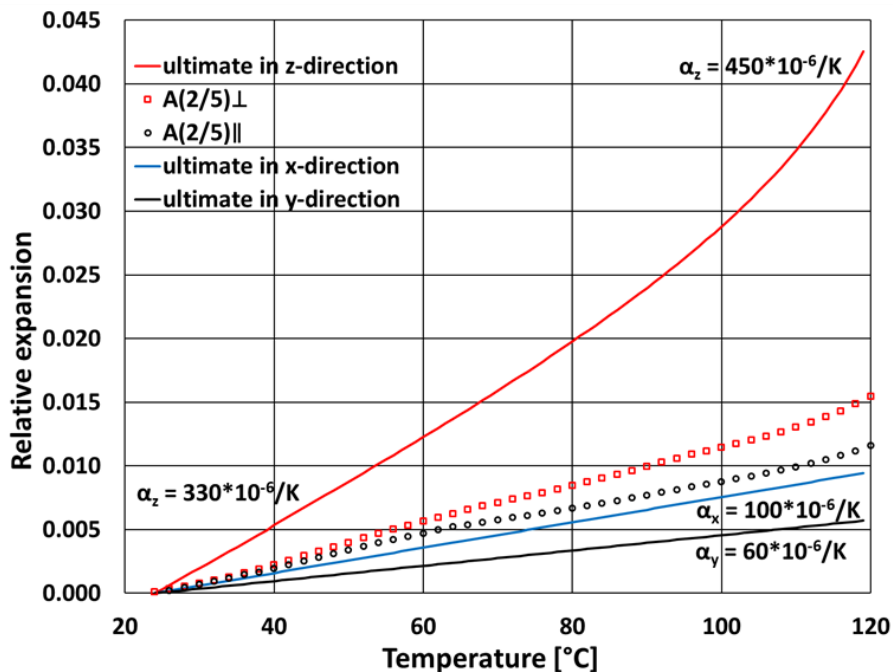
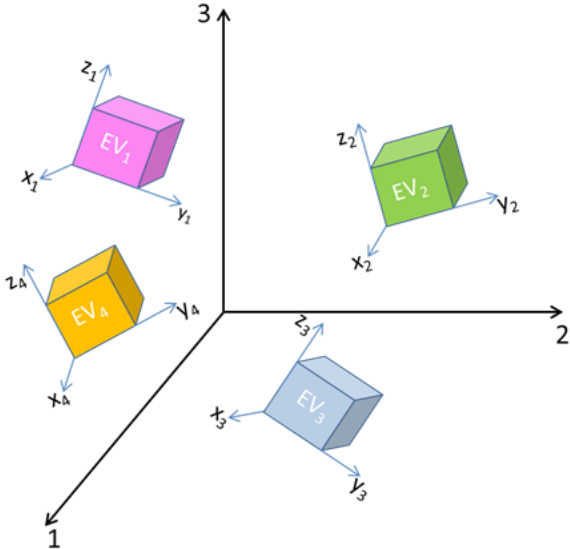


Fig. 21 Comparison of the 3 ultimate thermal expansions to the measured ones of sample A (2/5)

The ultimate thermal expansion described in the x-y-z-coordinate system of the EV does not coincide with the 1-2-3-coordinate system of the sample. Furthermore, there is an orientation distribution of EV within any part, Fig. 22.



**Fig. 22 Different orientation of elementary element volume cell (EV) with a part having the 1-2-3-coordinate system**

This requires that the local orientations of the EV have to be taken into account in terms of mean orientation. The procedure is analogous to Tucker’s method of describing fiber orientation distributions of plastic parts with 2<sup>nd</sup> order orientation tensors ( $a_{ik}$ ) [83]. Thus, for each fiber (spatial orientation of fiber axis) or EV (orientation of z-axis of EV) an orientation vector can be defined, Fig. 23, to quantify its spatial orientation with respect to the 1-2-3-coordinate system of the part, Eq. (20).

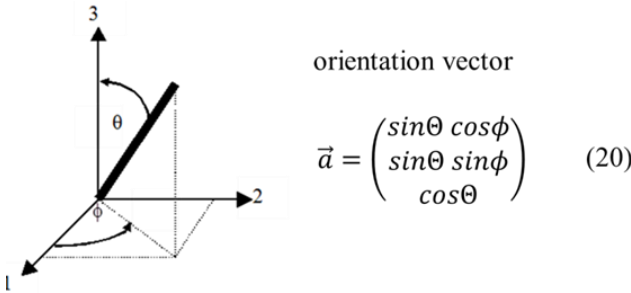


**Fig. 23 Demonstration of fiber orientation (or EV orientation) in term of angles  $\theta$  and  $\phi$  with definition of the orientation vector**

This approach allows for weighing the contributions of the ultimate CTE (x-y-z-coordinate system) to calculate the three CTE with respect to the 1-2-3-coordinate system of the part.

$$\begin{pmatrix} \alpha_1(T) \\ \alpha_2(T) \\ \alpha_3(T) \end{pmatrix} = \begin{pmatrix} a_{1x} & a_{1y} & a_{1z} \\ a_{2x} & a_{2y} & a_{2z} \\ a_{3x} & a_{3y} & a_{3z} \end{pmatrix} \begin{pmatrix} \alpha_x(T) \\ \alpha_y(T) \\ \alpha_z(T) \end{pmatrix} \quad (21)$$

where the orientation tensor is given by

$$(a_{ik}) = \begin{pmatrix} \sin^2 \theta \cos^2 \phi & \sin^2 \theta \sin \phi \cos \phi & \sin \theta \cos \theta \cos \phi \\ \sin^2 \theta \sin \phi \cos \phi & \sin^2 \theta \sin^2 \phi & \sin \theta \cos \theta \sin \phi \\ \sin \theta \cos \theta \cos \phi & \sin \theta \cos \theta \sin \phi & \cos^2 \theta \end{pmatrix} \quad (22)$$

Evaluating the thermal expansion behavior shows 20 to 50 % higher CTE perpendicular to MD than along MD, Table 8. This means that the blowing leads to a more pronounced molecular and crystalline orientation whereas the mold temperature has a rather minor effect. Interestingly, it was found that the CTE in the temperature range of 30°C to 60°C exceed the CTE in the temperature range of 70°C to 100°C by 30 to 40 %.

**Table 8 Effects of EBM processing parameter on Coefficients of Thermal Expansions CTE along and perpendicular to MD**

<b>Coefficients of Thermal Expansion in (<math>10^{-6} \cdot \text{K}^{-1}</math>)</b>						
<b>Sample</b>	<b><math>\alpha_{\parallel}</math> (30-60) °C</b>	<b><math>\alpha_{\perp}</math> (30-60) °C</b>	<b>Ratio <math>\alpha_{\perp} / \alpha_{\parallel}</math></b>	<b><math>\alpha_{\parallel}</math> (70-100) °C</b>	<b><math>\alpha_{\perp}</math> (70-100) °C</b>	<b>Ratio <math>\alpha_{\perp} / \alpha_{\parallel}</math></b>
<b>A (2/5)</b>	135±19	162±12	1.20	100±7	145±25	1.45
<b>B (3.4/5)</b>	112±13	162±14	1.45	79±9	132±9	1.67
<b>C (2/50)</b>	137±4	167±6	1.22	94±29	118±28	1.26
<b>D (3.4/50)</b>	98±10	132±19	1.48	120±6	177±20	1.54

Comparison of the calculated thermal expansion shows good agreement with measured data in the temperature range of 20 °C to 70 °C, Fig. 24.

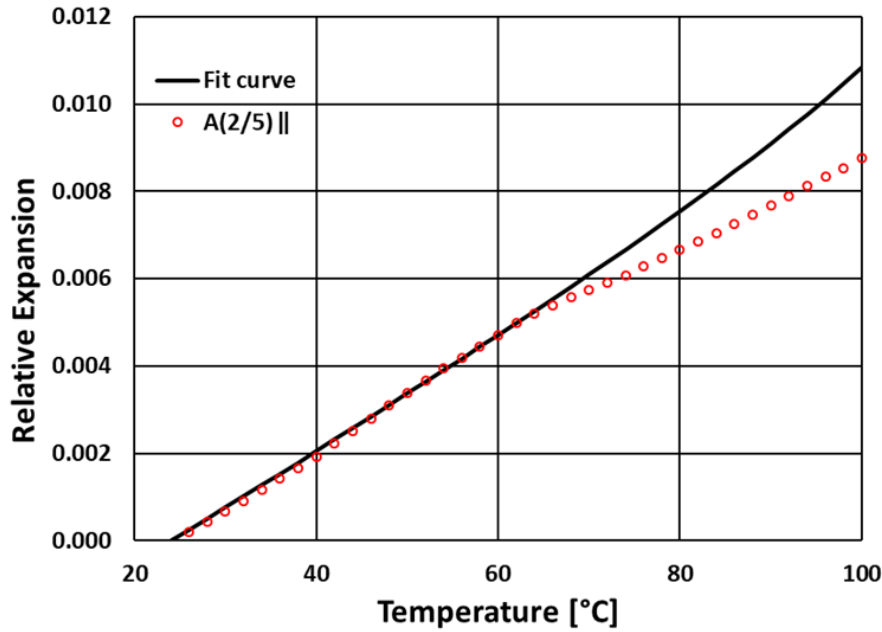


**Fig. 24** Fitting curve of the measured sample A (2/5) parallel to MD

Determining of the mean orientation angles in the corresponding temperature ranges show that mainly the angle  $\theta$  is decreased by approximately  $10^\circ$  (except for sample D) indicating some structural and orientational changes, Table 9. Furthermore, the angle  $\phi$  is found to be between  $50^\circ$  and  $60^\circ$  for both draw ratios and both mold temperatures showing that the contributions to thermal expansion are rather independent of orientations of the EV with respect to x- and y-direction.

**Table 9** Effects of EBM processing parameter on orientation angles  $\theta$  and  $\phi$

Sample	Orientation angle	Orientation angle in temperature range of fit		
		(~20-100) °C	(~20-70) °C	(70-100) °C
A(2/5)	$\theta$	<b>34.2</b>	<b>33.0</b>	<b>24.3</b>
	$\phi$	51.0	50.1	55.9
B(3.4/5)	$\theta$	<b>32.2</b>	<b>34.7</b>	<b>22.8</b>
	$\phi$	56.7	56.3	58.8
C(2/50)	$\theta$	<b>31.8</b>	<b>32.6</b>	<b>21.0</b>
	$\phi$	50.4	50.4	50.9
D(3.4/50)	$\theta$	<b>31.7</b>	<b>31.2</b>	<b>33.5</b>
	$\phi$	54.7	53.1	56.6

## 5 CONCLUSION

In this PhD thesis the process-structure-property relationship of extrusion blow molded high-density polyethylene products was investigated, and a model was developed that allows for taking into account the effects of the processing parameters (mold temperature and draw ratio) on thermal expansion behavior. The model is based on the lamellar structure of semi-crystalline polymers, and provides anisotropic ultimate coefficients of thermal expansion (CTE), in which the effects of processing parameters are accounted via crystallinity.

Statistical evaluation of dynamic mechanical analysis data showed that the influence of the variables such as flow direction, draw ratio, and mold temperature on storage moduli were statistically significant and process-dependent for specific temperature ranges. Statistically insignificant data indicates process-independent behavior, e.g. where the storage moduli were not influenced by the processing variables, were explained by relaxation processes during sample storage and at elevated measuring temperatures. The influence of the mold temperature was unaffected by these relaxation processes. Furthermore, the draw ratio and the mold temperature influenced the crystallinity of EBM products significantly: higher mold temperature and higher draw ratio caused higher crystallinities due to flow-induced orientation.

A new microindentation system to determine local viscoelastic material properties was successfully developed and implemented in a conventional DMA instrument. The measured complex moduli of four polymers are in accordance with bulk values and literature values. The comparison of annealed and unannealed samples showed that processing leads to large variations of local moduli, which is reflected in the larger standard deviations of unannealed samples. The adaption of a specially designed x-y-stage enabled spatial stiffness profiling. Thus, using the DMA microindentation along the cross-sectional thickness of EMB parts revealed that different processing parameters lead to different stiffness profiles. Furthermore, it could be shown that the measured complex moduli and crystallinities are lower near to the mold side compared to inner side and middle of the samples.

The orientation factors calculated from pole figures measured by wide angle X-ray revealed a low level of biaxiality with a slight tendency towards transverse direction for the polymer chain c-axis. The biaxiality increased for low mold temperature and high draw ratio. Biaxial orientation was confirmed by transmission electron micrographs showing no preferential lamellae orientation.

## 6 CONTRIBUTION TO SCIENCE AND PRACTICE

Extrusion blow molded (EBM) hollow plastic parts are indispensable in our daily life. As still over-dimensioned, their processing causes a higher material and energy consumptions. Due to future oil shortages and ecological reasons, the weight of EBM parts is to be reduced to the absolute minimum in order to access the potential materials, energy and costs savings. To reach this goal, the current EBM simulations have to be improved and optimized in terms of processing effects on the complex thermomechanical behavior and final deformation behavior of the parts. This requires the knowledge of the processing-structure-property relationship. A better understanding of the EBM process will then lead to optimum performing EBM parts.

This PhD thesis focused on the question how bulk and local processing-structure-property relationship of high-density polyethylene EBM parts are related to each other. A comprehensive study of the influence of the processing parameters - mold temperature and draw ratio - on structural and thermo-mechanical properties was performed. To interpret the results a model is presented to calculate the anisotropic coefficients of thermal expansion (CTE) as a function of crystallinity as a first step for predicting shrinkage and warpage. The following topics of this PhD thesis are considered as the most important contributions to both science and practice:

- 1) The results of the investigation of the bulk and local process-structure-property relationship of EBM high-density polyethylene products provide a better insight to the EBM process itself. Draw ratio and mold temperature influence the properties of EBM parts with respect to the flow direction significantly. Further, it was shown that their effects are reduced due to relaxation processes during storage time, and elevated temperatures during application. The cross-sectional property change goes along with crystallinity, which reflects the temperature gradient during cooling. Thus, measuring the cross-sectional stiffness profile provides both information about processing conditions and the mechanical performance of the part.
- 2) The effects of the investigated processing parameters can now be implemented in EBM simulation software to improve predictions of the thermo-mechanical behavior of EBM parts. This makes EBM production more sustainable.



- 3) The merging of microindentation and dynamic mechanical analysis allows for the determination of spatially resolved local surface properties and bulk properties using only one instrument.
- 4) The model to determine anisotropic thermal expansion and corresponding CTE introduce structural changes taking place within the material, thus leading to a better understanding of the performance of parts during application. Furthermore, this can be used to adjust processing conditions to optimize the performance of the EBM part.

## REFERENCES

- [1] M. Thielen, K. Hartwig, P. Gust. Blasformen von Kunststoff-Hohlkörpern, 2006, Hanser, München, Wien, ISBN-13:978-3-446-22671-5
- [2] D.G. Baird, D.I. Collais, Polymer processing, principles and design, 1998, Wiley, New York, ISBN 0-471-25453-3
- [3] T.A. Oswald, G. Menges, Material science of polymers for engineers, 3<sup>rd</sup> edition, 2012, Hanser, München, ISBN 978-1-56990-514-2
- [4] Grand View Research report, Blow molded plastics market analysis by technology, product, application and segment forecasts, 2014-2025, California, USA, August 2017, report ID: GVR-1-68038-574-8
- [5] S.L. Belcher, Practical Extrusion blow molding, 2010, CRC Press, ISBN 0-8247-1997-2
- [6] N.C. Lee, Understanding Blow Molding, 2000, Hanser, München, Wien, ISBN-13: 978-3-446-41265-1
- [7] N.C. Lee, Blow Molding Design Guide, 2nd ed., 2008, Hanser-Gardner Publications, ISBN 978-1-56990-426-8
- [8] D.V. Rosato, A.V. Rosato, D.P. DiMattia, Blow molding handbook, 2<sup>nd</sup> edition, 2004, Hanser, München, ISBN 3-446-22017-8
- [9] Feuerherm, <https://www.feuerherm-pwds.de>, last access 14 June 2018
- [10] P. Michels, D. Grommes, A. Oeckerath, D. Reith, O. Bruch, An integrative simulation concept for extrusion blow molded plastic bottles, *Finite Elem. Anal. Des.* 164 (2019) 69-78
- [11] L.H. Sperling, Introduction to physical polymer science, 4<sup>th</sup> edition, 2006, Wiley, New Jersey, ISBN: 13 978-0-471-70606-9
- [12] R.C. Allen, L. Mandelkern, On regimes I and II during polymer crystallization, *Polym. Bull.* 17 (1987), 473-480
- [13] B.A.G. Schrauwen, L.C.A. van Breemen, A.B. Spoelstra, L.E. Govaert, G.W.M. Peters, H.E.H. Meijer, Structure, deformation and failure of flow-oriented semicrystalline polymers, *Macromolecules* 37 (2004), 8618-8633
- [14] B.B. He, Two-dimensional X-ray diffraction, Wiley New Jersey, 2009, ISBN 978-0-470-22722-0
- [15] B. Wunderlich, Thermal Analysis, 1990, Academic Press. ISBN 978-0-124-11974-1
- [16] D.W. van Krevelen, Properties of Polymers, 3rd edition, 1997, Elsevier Scientific Publishing Company, Amsterdam, ISBN 978-0-444-59612-3
- [17] G.W. Ehrenstein, G. Riedel, P. Trawiel, Thermal analysis of plastics, 2004, Carl Hanser Verlag, München, ISBN 3-446-22673-7

- [18] G.H. Michler, F.J. Baltá-Calleja, Nano- and micromechanics of polymers, structure modification and improvement of properties, 2012, Carl Hanser Verlag, München, ISBN 978-3-446-42767-9
- [19] I.M. Ward, Structure and properties of oriented polymers, 2<sup>nd</sup> edition, 1997, Chapman and Hall, ISBN 0412-60880-4
- [20] R.S. Stein, The X-Ray Diffraction, Birefringence, and infrared dichroism of stretched polyethylene II: Generalized uniaxial crystal orientation, *J. Polym. Sci.*, 31 (1958), 327-334
- [21] R.S. Stein, The X-ray diffraction, birefringence, and infrared dichroism of stretched polyethylene. III: Biaxial orientation, *J. Polym. Sci.*, 31 (1958), 335-343
- [22] Z.W. Wilchinsky, Relationship between orientation parameters in biaxially oriented polymers, *J. Polym. Phys. Part A*, 4 (1966), 255-256
- [23] S. Nomura, H. Kawai, I. Kimura, M. Kagiya, General description of optical dichroic orientation factors for relating optical anisotropy of bulk polymer to orientation of structural units, *J. Polym. Phys. Part B*, 5 (1967), 479-491
- [24] W.R. Krigbaum, T. Adachi, J.V. Dawkins, Crystallite orientation distribution in biaxially oriented polyethylene, *J. Chem. Phys.*, 49 (1968) 1532-1542
- [25] S. Nomura, H. Kawai, I. Kimura, M. Kagiya, General description of orientation factors in terms of expansion of orientation distribution function in a series of spherical harmonics, *J. Polym. Phys. Part B*, 8 (1970), 383-400
- [26] P.H. Hermans, P. Platzek, Beiträge zur Kenntnis der Deformationsmechanismus und der Feinstruktur der Hydratzellulose, *Kolloid Z.* 88 (1939), 68-72
- [27] J.J. Hermans, P.H. Hermans, D. Vermaas, A. Weidinger, Quantitative evaluation of orientation in cellulose fibres from the X-ray fibre diagram, *Rec. Trav. Chim.* 65 (1946) 427-447
- [28] P.H. Hermans, J.J. Hermans, D. Vermaas, A. Weidinger, Deformation mechanism of cellulose gels. IV: General relationship between orientation of the crystalline and that of the amorphous portion, *J. Polym. Sci.* 3 (1948) 1-9
- [29] P.H. Hermans, D. Heikens, Orientation in cellulose fibers as derived from measurements of dichroism of dyed fibers, *Recl. Trav. Chim. Pays Bas* 71 (1952) 49-55

- [30] J.L. White., J.E. Spruiell, Specification of biaxial orientation in amorphous and crystalline polymers, *Polym. Eng. Sci.*, 21 (1981), 859-868
- [31] J.D. Ferry, Viscoelastic properties of polymers, Wiley, New York, 1980, ISBN 0471048941
- [32] W. Grellmann, S. Seidler, Polymer testing, 2<sup>nd</sup> edition, 2013, Hanser Verlag, München, ISBN 978-1-56990-548-7
- [33] W.C. Oliver, G.M. Pharr, An improved technique for determining hardness and elastic modulus using load and displacement sensing indentation experiments, *J. Mater. Res.* 7 (1992) 1564-1583
- [34] W.C. Oliver, G.M. Pharr, Measurement of hardness and elastic modulus by instrumented indentation: advances in understanding and refinements to methodology, *J. Mater. Res.* 19 (2004) 3-20
- [35] A.C. Fischer-Cripps, Critical review of analysis and interpretation of nanoindentation test data, *Surf. Coat. Tech.* 200 (2006) 4153-4165
- [36] M. Hardiman, T.J. Vaughan, C.T. McCarthy, The effects of pile-up, viscoelasticity and hydrostatic stress on polymer matrix nanoindentation, *Polym. Test.* 52 (2016) 157-166
- [37] S.R. Cohen, E. Kalfon-Cohen, Dynamic nanoindentation by instrumented nanoindentation and force microscopy: a comparative review, *Beilstein J. Nanotechn.* 4 (2013), 815-833
- [38] U.D. Schwarz, A generalized analytical model for the elastic deformation of an adhesive contact between a sphere and a flat surface, *J. Coll. Interf. Sci.* 261 (2003) 99–106
- [39] K.L. Johnson, K. Kendall, A.D. Roberts, Surface energy and contact of elastic solids, *Proc. R. Soc. Lond. A* 324 (1971), 301-313
- [40] D. Maugis, M. Barquins, Adhesive contact of a conical punch on an elastic half-space, *Journal de Physique Lettres* 42 (1981), 95-97
- [41] G. Kermouch, J.L. Loubet, J.M. Bergheau, Extraction of stress-strain curves of elastic-viscoplastic solids using conical/pyramidal indentation testing with application to polymers, *Mech. Mater.* 40 (2008), 271-283
- [42] G.M. Pharr, E.G. Herbert, Y. Goa, The indentation size effect: a critical examination of experimental observations and mechanical interpretations, *Annu. Rev. Mater. Res.* 40 (2010), 271-292
- [43] C. Han, Influence of the molecular structure on indentation size effect in polymers, *Mat. Sci. Eng. A* 527 (2010), 619-624
- [44] C. Han, S.H.R. Sanei, F. Alisafaei, On the origin of indentation size effects and depth dependent mechanical properties of elastic polymers, *J. Polym. Eng.* 36 (2015) 1-9

- [45] R.V.S. Tatiraju, C. Han, Rate dependence of indentation size effects in filled silicone rubber, *J. Mech. Mater. Struct.* 5 (2010), 277-288
- [46] C.C. White, M.R. VanLandingham, P.L. Drzal, N.-K. Chang, S.-H. Chang, Viscoelastic characterization of polymers using instrumented indentation. II. Dynamic Testing, *J. Polym. Sci. B Polym. Phys.* 43 (2005) 1812-1824
- [47] Keysight Technologies, Nano Indenter G200, prospect Keysight BP-6-20-17
- [48] B. Möglinger, V. Herrmann, C. Unseld, Quasi-static Indentation measurements: a tool for micro-mechanical investigations of interfaces in polymer materials, *Int. J. Pol. Anal. Charact.* 11 (2006) 405-418
- [49] S. Liparoti, V. Speranza, A. Sorrentino, G. Titomanlio, Mechanical properties distribution within polypropylene injection molded samples: effect of mold temperature under uneven thermal conditions, *Polymers* 2017, 9(11), 585-603
- [50] P. Enrique-Jimenez, J.F. Vega, J. Martínez-Salazar, F. Ania, A. Flores, Mapping the mechanical properties of poly(3-hydroxybutyrate-co-3-hydroxyvalerate) banded spherulites by nanoindentation, *Polymers* 2016, 8(10), 358-399
- [51] Y.K. Godovsky, Thermophysical properties of polymers, 1992, Springer Verlag, ISBN 978-3-642-51672-6
- [52] I.M. Ward, Developments in oriented polymers I: C.L. Choy, Thermal expansivity of oriented polymers, 1992, Applied Science Publishers, London, ISBN 0-85334-124-9
- [53] P.J. Barham, A. Keller, The problem of thermal expansion in polyethylene spherulites, *J. Mater. Sci.* 12 (1977), 2141-2148
- [54] G.T. Davis, R. K. Eby, J.P. Colson, Thermal expansion of polyethylene unit cell: effect of lamella thickness, *J. Appl. Phys.* 41 (1970), 4316-4326
- [55] C.L. Choy, F.C. Chen, K. Young, Negative thermal expansion on oriented crystalline polymers, *J. Polym. Sci. Polym. Phys.* 19 (1981), 335-352
- [56] C.L. Choy, S.P. Wong, K. Young, Temperature dependence of the thermal expansivity of polymer crystals: linear chain model, *J. Polym. Sci. Polym. Phys.* 22 (1984), 979-991
- [57] G.K. White, C.L. Choy, Thermal expansion and Grüneisen parameters of isotropic and oriented polyethylene, *J. Polym. Sci. Polym. Phys.* 22 (1984), 835-846
- [58] C.L. Choy, F.C. Chen, E.L. Ong, Anisotropic thermal expansion of oriented crystalline polymers, *Polymer* 20 (1979) 1191-1198

- [59] B. Möglinger, U. Fritz, Thermal properties of strained thermoplastic polymers, *Polym. Int.* 26 (1991) 121-128
- [60] M.D. Failla, J.M. Carella, Relaxation processes and structure of ultradrawn polyethylene, *J. Polym. Sci. Polym. Phys.* 26 (1988), 2433-2445
- [61] W.T. Mead, C.R. Desper, R.S. Porter, Physical mechanical properties of ultra-oriented high density polyethylene fibers, *J. Polym. Sci. Polym. Phys.* 17 (1979), 859-892
- [62] C.P. Buckley, N.G. McCrum, The thermal expansion of single-crystal texture linear polyethylene between 0 and -190°C, *J. Mater. Sci.* 8 (1973), 1123-1134
- [63] Technical datasheet, Lupolen 4261 AG, <https://www.lyondellbasell.com/en/polymers/p/Lupolen-4261AG/b060c35f-f786-4697-9508-c4be574677ec>, last access 17<sup>th</sup> September 2019
- [64] D. Grommes, O. Bruch, J. Geilen, Investigation of the influencing factors on the process-dependent elasticity modulus in extrusion blow molded plastic containers for material modelling in the finite element simulation, *AIP Conf. Proc.* 1779 (2016) 050013-1-050013-5
- [65] EN ISO 6721-1: Plastics - Determination of dynamic mechanical properties - Part 1: General principles
- [66] EN ISO 178: Plastics - Determination of flexural properties
- [67] EN ISO 11357-3: Plastics - Differential scanning calorimetry (DSC) - Part 3: Determination of temperature and enthalpy of melting and crystallization
- [68] J.S. Trent, Ruthenium tetroxide staining of polymers: new preparative methods for electron microscopy, *Macromolecules* 17 (1984) 2930-2931
- [69] M.R. Kamal, D. Kalyon, V. Tan, Anisotropy and dimensions of blow-molded polyethylene bottles, *Polym. Eng. Sci.* 22 (1982) 287-291
- [70] K.M. Seven, J.M. Cogen, J.F. Gilchrist, Nucleating agents for high-density polyethylene – a review, *Polym. Eng. Sci.* 5 (2016) 541-554
- [71] S. Liparoti, G. Titomanlio, S. Sorrentino, Analysis of asymmetric morphology evolutions in iPP molded samples induced by uneven temperature field, *AIChE J.* 62 (2016) 2699-2712
- [72] K. Cui, Z. Ma, N. Tian, F. Su, D. Liu, L. Li, Multiscale and multistep ordering of flow-induced nucleation of polymers, *Cem. Rev.* 118 (2018) 1840-1886
- [73] Z. Ma, L. Balzano, G.W. Peters, Dissolution and re-emergence of flow-induced shish in polyethylene with a broad molecular weight distribution, *Macromolecules* 49 (2016) 2724-2730

- [74] J. Hay, Introduction to instrumented indentation testing, *Exp. Tech.* (2009) 33, 66-72
- [75] <https://www.materialdatacenter.com>, last access 12<sup>th</sup> February 2019
- [76] <https://www.campusplastics.com>, last access 12<sup>th</sup> February 2019
- [77] J.L. White, J.E. Spruiell, The specification of orientation and its development in polymer processing, *Polym. Eng. Sci.* 23 (1983) 247-256
- [78] G.A.J. Orchard, G.R. Davies, I.M. Ward, The thermal expansion behavior of highly oriented polyethylene, *Polymer* 25 (1984) 1203-1210
- [79] N.J. Capiati, R.S. Porter, Dimensional changes in ultradrawn polyethylene, *J. Polym. Sci. Polym. Phys.* 15 (1977) 1427-1434
- [80] F.C. Stehling, L. Mandelkern, The glass temperature of linear polyethylene, *Macromolecules* 3 (1970) 242-252
- [81] J.L. Kardos, J. Raison, S. Piccarolo, Prediction and measurement of the thermal expansion coefficient of crystalline polymers, *Polym. Eng. Sci.* 19 (1979) 1000-1009
- [82] H.G. Elias, *Polymere: von Monomeren und Makromolekülen zu Werkstoffen*, 1996, Hüthig und Wepf Verlag: Zug, Heidelberg, Oxford, ISBN 3-8252-8107-8
- [83] R.S. Bay, C.L. Tucker III, Fiber orientation in simple moldings. Part II: experimental results, *Polym. Comp.* 13 (1992) 332-341

## LIST OF FIGURES

- Fig. 1 Principle of EBM [1]
- Fig. 2 Typical DSC-melting curve and crystallite distribution of a semi-crystalline polymer [17]
- Fig. 3 Sinusoidal oscillation of the input ( $\varepsilon(t)$ ) and the response signal ( $\sigma(t)$ ) with the phase angle  $\tan\delta$  (left); diagram of the modulus  $E^*$  in the complex plane (right) [32]
- Fig. 4 Flow chart of the methodology and techniques employed in the PhD thesis
- Fig. 5 Dendrogram: a cluster analysis of storage moduli (Minitab 14, Minitab Inc.)
- Fig. 6 Statistical  $p$ -values of the variables over temperature
- Fig. 7 Trend lines of the relative effects of statistically significant parameters over the measuring temperature
- Fig. 8 Process-dependent local cross-sectional crystallinities of the EBM part, where 0  $\mu\text{m}$  represents the mold side and 1000  $\mu\text{m}$  the inner side correspond to fits using a second order polynomial
- Fig. 9 Special indenter holders for (a) tungsten needle and (b) diamond indenters
- Fig. 10 Specially developed x-y-stage with a laser positioning system for spatial resolution of microindentations
- Fig. 11 Measured complex moduli along the cross sectional area of an unannealed HDPE tensile test bar (dots) with second order polynomial fit as trend line (dashed line)
- Fig. 12 Effects of mold temperature and draw ratio on local crystallinities and complex moduli along the cross-section of the EBM part, second order polynomial fits are displayed as trend lines
- Fig. 13 Pole figures for a-axis for the samples (2/50), left, and (3.4/5), right
- Fig. 14 White-Spruiell isosceles triangle of c-axis of orientation factors derived from X-ray diffraction, the dashed line represents biaxial orientation
- Fig. 15 Transmission electron micrographs of the (3.4/5)-sample, (a) parallel to MD close to the mold side, (b) parallel to TD close to the mold side, (c) parallel to MD close to the inner side, (d) parallel to TD close to the inner side
- Fig. 16 Sketch of the elementary volume unit cell (EV) for semi-crystalline polymers
- Fig. 17 The 4 stages of modelling thermal expansion to calculate anisotropic coefficients of thermal expansion (CTE) in x-, y- and z-direction
- Fig. 18 Calculation of the ultimate anisotropic CTE's as function of the crystallinity



- Fig. 19 Measured thermal expansion parallel ( $\parallel$ ), left, and perpendicular ( $\perp$ ), right, to the extrusion direction (the curves A, B, and C are vertically shifted by a constant value of 0.75 %, 0.5 %, and 0.25 %, respectively, for clarity reasons)
- Fig. 20 (a) Temperature dependent crystallinities as a function of temperature for the EBM-samples, (b) fitted partial melting, (c) resulting fit parameters for modelling of CTE
- Fig. 21 Comparison of the ultimate thermal expansions to the measured ones of sample A (2/5)
- Fig. 22 Different orientation of elementary element volume cell (EV) with a part having the 1-2-3-coordinate system
- Fig. 23 Demonstration of fiber orientation (or EV orientation) in term of angles  $\theta$  and  $\phi$  with definition of the orientation vector
- Fig. 24 Fitting curve of the measured sample A (2/5) parallel to MD

## LIST OF TABLES

- Table 1 Structure qualification with corresponding scale [18]
- Table 2 CTE of PE and PP of crystalline phase, amorphous phase and produced parts
- Table 3 Measuring methods, determined quantities, instruments and standards
- Table 4 Crystallinities and  $p$ -values for parameters mold temperature and draw ratio
- Table 5 Contact areas (projected area) of the used indenter geometries
- Table 6 Comparison of complex moduli (MPa) of the investigated polymers determined with the 4 indenter geometries, three-point bending, and Young's moduli from literature [75,76]
- Table 7 Coefficient of Thermal Expansions CTE and Young's moduli of crystalline and amorphous phase of PE taken from literature [52-62,78-82]
- Table 8 Effects of EBM processing parameter on Coefficients of Thermal Expansions CTE along and perpendicular to MD
- Table 9 Effects of EBM processing parameter on orientation angles  $\theta$  and  $\phi$

## ABBREVIATIONS

AFM	Atomic force microscopy
ANOVA	Analysis of Variance
AWDS	Axial wall thickness distribution system
CSM	Continuous stiffness measurement
CTE	Coefficient of thermal expansion
DMA	Dynamic mechanical analysis
DSC	Differential scanning calorimetry
EBM	Extrusion blow molding
EV	Elementary volume unit cell
HDPE	High density polyethylene
INI	Instrumented nano-indentation
IR	Infrared
ISE	Indentation size effect
LM	Light microscopy
MD	Machine direction
$M_w$	Molecular weight
MWD	Molecular weight distribution
ND	Normal direction
NMR	Nuclear magnetic resonance
PBT	Polybutylene terephthalate
PC	Polycarbonate
PE	Polyethylene
PhD	Doctor of philosophy
PP	Polypropylene
<i>p</i> -value	Probability value
PWDS	Partial wall thickness distribution system
SAXS	Small angle X-Ray diffraction
SEM	Scanning electron microscopy
TD	Transverse direction
TEM	Transmission electron microscopy
TMA	Thermomechanical analysis
TPU	Thermoplastic polyurethane
USA	United states of America
WAXD	Wide angle X-Ray diffraction
XRD	X-Ray diffraction

## SYMBOLS

$A$	Contact area
$a_{ik}$	2 <sup>nd</sup> order orientation tensor
$b_0$	Width of EV
$b_x$	Equilibrium width in x-direction
$b_{am}^{fr,x}$	Width amorphous phase, free expansion
$b_{cr}^{fr,x}$	Width crystalline phase, free expansion
$c_0$	Thickness of EV
$c_y$	Equilibrium thickness in y-direction
$c_{am}^{fr,y}$	Height amorphous phase, free expansion
$c_{cr}^{fr,y}$	Height crystalline phase, free expansion
$dh$	Penetration depth
$E$	Elastic modulus
$E^*$	Complex modulus
$E'$	Storage modulus
$E''$	Loss modulus
$E_{am,x,y,z}$	Young's modulus of amorphous phase in x-, y- and z-direction
$E_{cr,x}^\perp$	Young's modulus perpendicular to crystal chain axis in x- direction
$E_{cr,y}^\perp$	Young's modulus perpendicular to crystal chain axis in y- direction
$E_{cr,z}^\parallel$	Young's modulus along crystal chain axis in z-direction
$E_r$	Reduced modulus
$E_s$	Elastic modulus of sample
$F$	Force
$f^B$	Biaxial orientation function
$f_{MD}$	Orientation factor in machine direction
$f_{TD}$	Orientation factor in transverse direction
$\Delta H_m$	Heat of fusion
$\Delta H_m^0$	Heat of fusion of a 100 % crystalline polymer
$h$	Displacement
$h_{max}$	Maximum indentation displacement
$h_z$	Final length of EV
$h_0$	Height of EV
$h_{0,cr}$	Height of crystalline lamellae in EV
$h_{am}^{fr,z}$	Length amorphous phase, free expansion
$h_{cr}^{fr,z}$	Length crystalline phase, free expansion
$I_{hkl}$	Integrated intensity for a crystalline plane (XRD)
$k$	Fitting parameter
$L$	Length
$L_0$	Initial length

$n$	Fitting parameter
$P$	Load
$P_{static}$	Static preload
$R$	Radius
$R^2$	Coefficient of determination
$S$	Stiffness
$t$	Time
$T$	Temperature
$T_g$	Glass transition temperature
$T_{im}$	Onset melting temperature
$T_m$	Melting temperature
$T_{pm}$	Melting peak point
$T_{pole}$	Pole temperature
$V(T_0)$	Initial EV-volume
$X_{cr}$	Degree of crystallinity
$X_{cr,0}$	Initial crystallinity
$\parallel$	parallel
$\perp$	perpendicular

## GREEK SYMBOLS

$\alpha$	Coefficient of thermal expansion (CTE)
$\alpha_{am}$	CTE of amorphous region
$\alpha_{am,x}$	CTE of amorphous phase in x-direction
$\alpha_{am,y}$	CTE of amorphous phase in y-direction
$\alpha_{am,z}$	CTE of amorphous phase in z-direction
$\alpha_{cr}^{\parallel}$	CTE of crystalline region along the crystallographic c-axis
$\alpha_{cr,z}^{\parallel}$	CTE along crystal chain axis in z-direction
$\alpha_{cr}^{\perp}$	CTE of crystalline region perpendicular to the crystallographic c-axis
$\alpha_{cr,x}^{\perp}$	CTE perpendicular to crystal chain axis in x-direction
$\alpha_{cr,y}^{\perp}$	CTE perpendicular to crystal chain axis in y-direction
$\alpha_{x,y,z}$	CTE in x-, y-, z-direction
$\delta$	Phase angle
$\tan\delta$	Loss factor
$\varepsilon_0$	Initial strain
$\varepsilon(T)$	Temperature induced strain
$\varepsilon(\omega)$	Sinusoidal deformation
$\Theta$	Half space angle indenter
$\theta$	Tilt angle

$\nu_s$	Poisson ratio sample
$\pi$	Pi
$\sigma_0$	Initial stress
$\sigma(\omega)$	Sinusoidal stress
$\phi$	Angle between lattice and laboratory axis, rotation angle
$\omega$	Angular frequency

## PUBLICATIONS, POSTERS, AND PRESENTATIONS

Publications in context of this doctoral work:

- E. Ramakers-van Dorp, T. Haenel, F. Sturm, B. Möglinger, B. Hausnerova, On merging DMA and microindentation to determine local mechanical properties. *Polym. Test.* 68 (2018) 359-364
- E. Ramakers-van Dorp, T. Haenel, D. Ciongwa, B. Möglinger, B. Hausnerova, Development of an advanced dynamic microindentation system to determine local viscoelastic properties of polymers. *Polymers* 11 (2019) 833-846
- E. Ramakers-van Dorp, C. Blume, T. Haedecke, V. Pata, D. Reith, O. Bruch, B. Möglinger, B. Hausnerova, Process-dependent structural and deformation properties of extrusion blow molding parts. *Polym. Test.* 77 (2019) 105903,
- E. Ramakers-van Dorp, B. Eger, C. Raschen, M. Urbanek, B. Möglinger, B. Hausnerova, Local process-dependent structural and mechanical properties of extrusion blow molded high-density polyethylene parts. Submitted to *Polym. Test.*, September 2019
- E. Ramakers-van Dorp, B. Möglinger, B. Hausnerova, Thermal expansion of semi-crystalline polymers: Anisotropic thermal strain and crystallite orientation. Submitted to *Polymer*, November 2019

Conference Publications:

- A new evaluation method to determine depth depending properties of visible light curing resin based composites, T. Haenel, M. Dopadlo, R.B.T. Price, B. Hausnerova, J. Steinhaus, E. Ramakers-van Dorp, B. Möglinger. IADR 2015, Antalya, Turkey, poster presentation
- A new approach to model thermal expansion of semi-crystalline polymers, E. Ramakers-van Dorp, T. Haenel, J. Steinhaus, D. Reith, O. Bruch, B. Möglinger, B. Hausnerova. PPS 2015, Graz, Austria, oral poster presentation
- Curing and postcuring of dental materials, E. Ramakers-van Dorp. Application Seminar Perkin Elmer, 2015, Hamburg, Germany, oral presentation
- A new approach to model thermal expansion of semi-crystalline polymers, E. Ramakers-van Dorp, B. Möglinger, B. Hausnerova. PPS 2017, Dresden, Germany, oral presentation

- New development of a microindentation system to determine mechanical properties of polymers, E. Ramakers-van Dorp, T. Haenel, F. Sturm, B. Möglinger, B. Hausnerova. DVSPM 2017, Wien, Austria, oral poster presentation
- Quantitative analysis of relationship between extrusion blow molding process parameters and deformation properties, E. Ramakers-van Dorp, B. Möglinger, B. Hausnerova. IRF 2018, Lisbon, Portugal, oral poster presentation
- Development of an advanced microindentation method to determine local viscoelastic properties of polymers, E. Ramakers-van Dorp, T. Haenel, D. Ciongwa, B. Möglinger, B. Hausnerova. NRC 2019, Goteborg, Sweden, oral poster presentation
- Microindentation with conventional dynamic mechanical analysis to determine local mechanical properties of polymers, E. Ramakers-van Dorp. testXpo2019, Ulm, Germany, oral presentation

# CURRICULUM VITAE

**Date and place of birth** February 14<sup>th</sup>, 1974 in Heerlen, the Netherlands

**Permanent Address** Von-Liebigstrasse 20  
D-53359 Rheinbach, Germany  
Tel.: (+49) 2241 865 522  
e-mail: esther.vandorp@h-brs.de

## Education

since 01/2014 PhD studies at Thomas Bata University Zlín, Faculty of Technology, Department of Production Engineering

09/1995-09/1998 Chemical Engineering at Hogeschool Limburg, Heerlen, the Netherlands, Faculty of Technology

## Work experience

since 05/1999 Scientific assistant at University of Applied Sciences Bonn-Rhein-Sieg, Rheinbach, Germany, Department of Natural Sciences

Laboratory Supervisor: Polymer Processing; Polymer Thermal Analysis; Polymer Testing

Practical Supervisor: Polymers and Composites

since 2003 Research assistant polymers research group at University of Applied Sciences Bonn-Rhein-Sieg, Rheinbach, Germany

since 2010 Project engineer at University of Applied Sciences Bonn-Rhein-Sieg, Germany



Esther Ramakers-van Dorp, Ph.D.

**Process-Induced Thermal and Viscoelastic Behavior  
of Extrusion Blow Molded Parts**

Procesem indukované tepelné a viskoelastické vlastnosti dílů vyrobených  
vytlačovacím vyfukováním

Doctoral Thesis Summary

Published by: Tomas Bata University in Zlín,  
nám. T. G. Masaryka 5555, 760 01 Zlín.

Edition: published electronically

Typesetting by: Esther Ramakers-van Dorp, Ph.D.

This publication has not undergone any proofreading or editorial review.

Publication year: 2019

First Edition

ISBN 978-80-7454-892-5

